

Supplementary Material to:

Hyperbolic topological band insulators

David M. Urwyler,¹ Patrick M. Lenggenhager ,^{1, 2, 3} Igor Boettcher ,^{4, 5}
 Ronny Thomale ,⁶ Titus Neupert ,¹ and Tomáš Bzdušek ,^{2, 1, *}

¹*Department of Physics, University of Zurich, Winterthurerstrasse 190, 8057 Zurich, Switzerland*

²*Condensed Matter Theory Group, Paul Scherrer Institute, 5232 Villigen PSI, Switzerland*

³*Institute for Theoretical Physics, ETH Zurich, 8093 Zurich, Switzerland*

⁴*Department of Physics, University of Alberta, Edmonton, Alberta T6G 2E1, Canada*

⁵*Theoretical Physics Institute, University of Alberta, Edmonton, Alberta T6G 2E1, Canada*

⁶*Institut für Theoretische Physik und Astrophysik,*

Universität Würzburg, 97074 Würzburg, Germany

(Dated: October 31, 2022)

Contents

I. Geometry of the hyperbolic plane.	2
II. Geometry of $\{p, q\}$ tessellations.	3
III. Reduced Kane-Mele model.	4
IV. Hyperbolic Bloch Hamiltonian.	6
V. Flake Hamiltonian in position space.	7
VI. Considered system sizes in the flake geometry.	8
VII. Bulk density of states and integrated boundary density of states for the flake Hamiltonian.	9
VIII. Real-space invariants.	10
IX. Gaussian projector operator.	12
X. Models of disorder.	13
XI. Hyperbolic Bloch Hamiltonians of the studied models	14
XII. Wilson-loop extraction of topological band invariants	16
XIII. Extraction of the edge mode dispersion	18
XIV. Group velocity of the chiral edge states in hyperbolic Haldane model	23
XV. Phase diagram of the hyperbolic Haldane Bloch Hamiltonian at half-filling and $\Phi = \pi/2$	24

* corresponding author: tomas.bzdusek@psi.ch

I. Geometry of the hyperbolic plane.

We adopt the Poincaré-disk representation of the hyperbolic plane, i.e., as the unit disk in the complex plane, $\mathbb{D} = \{z \in \mathbb{C} \mid |z| < 1\}$, with the hyperbolic metric given by

$$ds^2 = (2\kappa)^2 \frac{dz d\bar{z}}{(1 - z\bar{z})^2}, \quad (\text{S1})$$

where κ is a unit of length and the bar in \bar{z} indicates complex conjugation. With this choice, the Gaussian curvature equals $K = -\kappa^2$. In our work, we fix $\kappa = 1/2$ (leading to curvature $K = -4$). With this convention,

$$d(z_1, z_2) = \frac{1}{2} \operatorname{arccosh} \left[1 + \frac{2|z_1 - z_2|^2}{(1 - |z_1|^2)(1 - |z_2|^2)} \right] \quad (\text{S2})$$

determines the geodesic distance for a pair of points $z_{1,2} \in \mathbb{D}$ [17].

We briefly investigate geometric aspects of a disk with radius $0 < R < 1$ in the complex plane, labelled \mathbb{D}_R . Its surface area is computed as

$$S(R) = \int_0^{2\pi} d\phi \int_0^R dr \frac{r}{(1 - r^2)^2} = \frac{\pi R^2}{1 - R^2}. \quad (\text{S3})$$

The hyperbolic distance from the center to the boundary of the disk is

$$d(0, R) = \int_0^R \frac{dr}{(1 - r^2)} = \frac{1}{2} \operatorname{arccosh} \left(\frac{1 + R^2}{1 - R^2} \right) = \operatorname{artanh} R, \quad (\text{S4})$$

and its perimeter is

$$p(R) = \int_0^{2\pi} d\phi \frac{R}{(1 - R^2)} = \frac{2\pi R}{1 - R^2}. \quad (\text{S5})$$

It is easily verified that $p(R)/d(0, R) > 2\pi$ (for perimeter) and $S(R)/d^2(0, R) > \pi$ (for surface area), as expected for a negatively curved space.

II. Geometry of $\{p, q\}$ tessellations.

We determine the distance $d_1^{\{p,q\}}$ of nearest-neighbor vertices of the $\{p,q\}$ lattice. For that purpose, we consider a triangle ABC where: A is the center of a regular p -sided polygon (a ‘ p -gon’, for short), B is one of the p -gon’s vertices, and C is a point that lies on the boundary of the p -gon at the middle of an edge connecting to B . Note that the hyperbolic length of the triangle side $|BC| = d_1^{\{p,q\}}/2$. The internal angles of triangle ABC at vertices A , B , and C are identified as $\alpha = \pi/p$, $\beta = \pi/q$, and $\gamma = \pi/2$, respectively. According to the hyperbolic law of cosines [27],

$$\cosh\left(\frac{|BC|}{\kappa}\right) = \frac{\cos\alpha + \cos\beta \cos\gamma}{\sin\beta \sin\gamma} = \frac{\cos\frac{\pi}{p}}{\sin\frac{\pi}{q}}, \quad (\text{S6})$$

which implies $d_1^{\{8,3\}} = \operatorname{arcosh}(\cos\frac{\pi}{8}/\sin\frac{\pi}{3}) \approx 0.36352$ for our choice $\kappa = 1/2$. Next, the distance $|AB| = r^{\{p,q\}}$ from the center of the p -gon to its vertex is also determined from the law of cosines,

$$\cosh\left(\frac{|AB|}{\kappa}\right) = \frac{\cos\gamma + \cos\alpha \cos\beta}{\sin\alpha \sin\beta} = \frac{1}{\tan\frac{\pi}{p} \tan\frac{\pi}{q}}, \quad (\text{S7})$$

leading to $r^{\{8,3\}} = \operatorname{arcosh}[1/(\tan\frac{\pi}{8} \tan\frac{\pi}{3})]/2 \approx 0.430353$.

If the center of the p -gon is placed at the center of the Poincaré disk ($z = 0$), then Eq. (S4) governs the complex coordinates of the p -gon vertices, $|z_B^{\{p,q\}}| = \tanh(r^{\{p,q\}})$, leading to $|z_B^{\{8,3\}}| \approx 0.405616$. The information obtained thus far is sufficient to find the complex coordinates $\{z_{(\emptyset,a)}\}_{a=1}^{n_{\text{cell}}}$ (where $n_{\text{cell}} = 16$) of all sites of the $\{8,3\}$ lattice which reside inside the Bolza cell centered at $z = 0$ (listed in Supplementary Table S1). For later purposes, we use Eq. (S2) to also determine the distance of next-nearest-neighbor sites as

$$d_2^{\{p,q\}} = d\left(|z_B^{\{p,q\}}|e^{2\pi i/p}, |z_B^{\{p,q\}}|e^{-2\pi i/p}\right), \quad (\text{S8})$$

which leads to $d_2^{\{8,3\}} = \operatorname{arcosh}(1 + \frac{2\sqrt{2}}{3})/2 \approx 0.641645$.

site label a	1	2	3	4
coordinate $z_{(\emptyset,a)}$	$0.374741 + 0.155223i$	$0.155223 + 0.374741i$	$-0.155223 + 0.374741i$	$-0.374741 + 0.155223i$
site label a	5	6	7	8
coordinate $z_{(\emptyset,a)}$	$-0.374741 - 0.155223i$	$-0.155223 - 0.374741i$	$0.155223 - 0.374741i$	$0.374741 - 0.155223i$
site label a	9	10	11	12
coordinate $z_{(\emptyset,a)}$	$0.610313 + 0.252800i$	$0.252800 + 0.610313i$	$-0.252800 + 0.610313i$	$-0.610313 + 0.252800i$
site label a	13	14	15	16
coordinate $z_{(\emptyset,a)}$	$-0.610313 - 0.252800i$	$-0.252800 - 0.610313i$	$0.252800 - 0.610313i$	$0.610313 - 0.252800i$

TABLE S1. **Coordinates of the sites in the Bolza cell.** The table lists the complex coordinates of the 16 sites of the $\{8,3\}$ lattice which belong to the innermost Bolza cell (centered at $z = 0$), represented inside the Poincaré disk with radius 1. For derivation of these values, and for the meaning of the subscript “ (\emptyset, a) ”, see Methods.

The Gauss-Bonnet theorem [48] relates surface area S^P of a geodesic p -sided polygon P in space of constant curvature K to its internal angles $\{\alpha_j\}_{j=1}^p$,

$$\sum_{j=1}^p (\pi - \alpha_j) = 2\pi - KS^P. \quad (\text{S9})$$

The elementary cell of the $\{p, q\}$ lattice is a regular geodesic p -gon with all internal angles of size $\alpha = 2\pi/q$. It follows from Eq. (S9) that the surface area of the elementary p -gon is

$$S^{\{p,q\}} = \pi \frac{(p-2)(q-2)-4}{4q}. \quad (\text{S10})$$

We obtain $S^{\{8,3\}} = \pi/6$, while the area of the Bolza cell (p -gon of $\{8,8\}$ lattice) is six times larger, $S^{\text{Bolza}} = \pi$. The ratio

$$\tilde{N}_{\text{UC}}(R) = \frac{S(R)}{S^{\text{Bolza}}} = \frac{R^2}{1-R^2} \quad (\text{S11})$$

gives an approximate number of Bolza cells that fit into a disk with radius R in the complex plane.

III. Reduced Kane-Mele model.

To avoid complications that arise from non-trivial spin holonomy in curved spaces, we construct the *reduced* Kane-Mele (rhKM) model through the following simplification [cf. Supplementary Fig. S1]: instead of taking the negative curvature to be constant inside the Bolza cell, we consider a continuous deformation where all the curvature becomes concentrated at the corners of the cell (cyan dots in Supplementary Fig. S1) while the manifold becomes flat everywhere else. Then, the Bolza cell essentially becomes a Euclidean regular octagon (black outline in Supplementary Fig. S1). [Note that the adjacent Bolza cells (dashed frames in Supplementary Fig. S1) seemingly overlap one another, but this is consistent with the -4π quantum of curvature at the vertex.] Then there exists a unique arrangement of the 16 sites of the $\{8, 3\}$ lattice (blue frame in Supplementary Fig. S1) within the octagon such that (1) all pairs of NN sites have the same distance, and (2) the eightfold rotation and mirror symmetries of the octagon are preserved.

The advantage of the deformed model is that the NN hopping of electrons occurs within regions of zero curvature, allowing us to construct the Rashba SOC terms using the procedure familiar from the flat Euclidean space. Namely, we imagine the presence of a substrate that creates a constant electric field E_z perpendicular to the 2D plane of the system. As the spinful electron hops (within the locally flat region) between a pair of NN sites $b \leftrightarrow a$ (represented in Supplementary Fig. S1 with thin pink/orange/brown arrows), characterized by displacement vector $\mathbf{r}_{ba} = \mathbf{r}_b - \mathbf{r}_a$ [where the vectors are decomposed into local (x, y) coordinates that run rightwards/upwards inside the illustration in Supplementary Fig. S1], the electron perceives in its moving reference frame a magnetic field $\mathbf{B}_{ba} \propto \mathbf{r}_{ba} \times \mathbf{E}$ [where $\mathbf{E} = (0, 0, E_z)$, and \mathbf{r}_{ba} has been supplemented with vanishing component in the third direction]. The obtained magnetic fields are in-plane vectors [indicated for several hopping processes in Supplementary Fig. S1 with thick pink/orange/brown arrows], which are characterized by their direction θ_{ba} . The corresponding Rashba term added to the rhKM Hamiltonian is

$$\mathcal{H}_{ba} = i\lambda_R [\cos(\theta_{ba})\sigma_x + \sin(\theta_{ba})\sigma_y]. \quad (\text{S12})$$

By repeating the above procedure for hopping $a \leftrightarrow b$, we find that $\mathcal{H}_{ab} = -\mathcal{H}_{ba}$, which is compatible with time-reversal symmetry $\mathcal{T} = i\sigma_y \mathcal{K}$.

In the corresponding code in the enclosed data repository [60] (see also Supplementary Note XI), we label the angles θ_{ba} as one of $\{\alpha(j), \beta(j), \gamma(j)\}_{j=1}^8$ (illustrated in pink/orange/brown in Supplementary Fig. S1); the three symbols distinguish respectively the Rashba terms on NN bonds (1) along the inner elementary (blue) octagon, (2) directed towards the corners of the large (black) octagon, and (3) crossing the boundary of the large octagon.

Let us emphasize that the interpretation with the non-homogeneous curvature is only adopted to *construct* the Hamiltonian elements in Eq. (S12). When discussing the geometry of the system in the subsequent text, we still assume the 16 sites of the inner Bolza cell to be located at the complex coordinates listed in Supplementary Table S1, while keeping the Hamiltonian elements derived above.

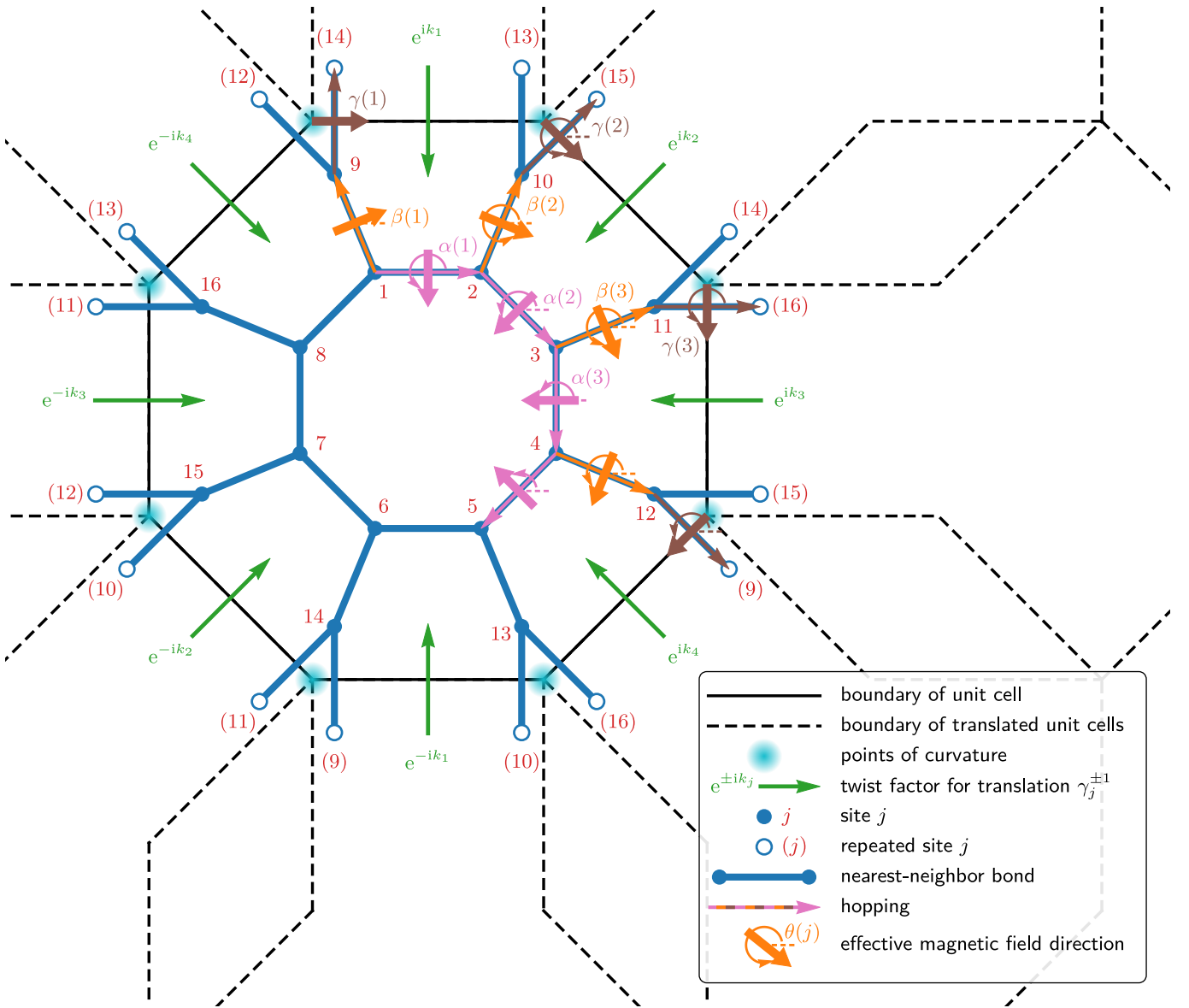


FIG. S1. Geometry of the reduced Kane-Mele model. (For details of the construction, see Methods). In the reduced hyperbolic Kane-Mele model, the lattice is deformed such that all the negative curvature is concentrated at the corners (cyan dots) of the unit cell (the Bolza cell; deformed into the black octagon). As a consequence, space is flat everywhere except at those points (octagon corners,) and the neighbouring unit cells (dashed black octagons) seem to overlap in our representation of the lattice. The unit cell contains 16 sites (blue dots labelled by red numbers). Assuming an electric field due to the substrate pointing out of the plane, hopping between two sites (pink, orange and brown thin arrows) leads to an effective magnetic field pointing in the direction of the corresponding thick arrow (of the same color). This direction is parametrized by an angle $\theta(j)$, where $\theta = \alpha, \beta, \gamma$ depending on whether the hopping is on the inner ring, in the radial direction, or across different Bolza unit cells, respectively, and $j \in \{1, \dots, 8\}$ enumerates those nearest-neighbour bonds. Assuming first that we set the alternating on-site potential to $M = 0$, the constructed model preserves time-reversal symmetry \mathcal{T} , the eightfold rotation symmetry with respect to the center of the Bolza cell (corresponding to symmetry ‘ R ’ in the Supplementary Material to Ref. [9]), the mirror symmetry with respect to lines connecting antipodal corners of the unit cell (symmetry ‘ S ’ in Ref. [9]), and the mirror symmetry with respect to lines connecting centers of antipodal edges of the unit cell (composition of R and S). However, the model breaks the threefold rotation symmetry with respect to any site of the $\{8, 3\}$ lattice (symmetry ‘ U ’ in Ref. [9]), as is apparent from the varying geometrical distortions of the six elementary (blue) octagons in the Bolza unit cell. The on-site $\pm M$ term further breaks R (but not \mathcal{T} and S) symmetry. [Note that in the main text we use symbol ‘ R ’ to indicate a $(\pi/2)$ -rotation around the center of the Bolza cell, whereas the same symbol is used by Ref. [9] to indicate a $(\pi/4)$ -rotation around the same point.]

IV. Hyperbolic Bloch Hamiltonian.

To obtain the hyperbolic Bloch Hamiltonian $\mathcal{H}(\mathbf{k})$ from tight-binding Hamiltonian \mathcal{H} in position space, we replace the infinite lattice by a single Bolza cell with identified antipodal boundaries [pairs of colored edges in Fig. 1(a)] [9]. To implement the twisted boundary conditions, tunnelling amplitudes (t) for hopping process that cross edges displaced by $\gamma_j^{\pm 1}$ are multiplied by phase factors $e^{\pm ik_j}$. Since there are four phases $\{k_j\}_{j=1}^4 \equiv \mathbf{k}$, it follows that $\mathcal{H}(\mathbf{k})$ is defined over a 4D BZ. For models on the $\{8, 3\}$ lattice, the presence of $n_{\text{cell}}=16$ sites per Bolza cell implies that $\mathcal{H}(\mathbf{k})$ is a matrix of dimensions $D_{\text{Bloch}}=n_{\text{cell}}$ ($D_{\text{Bloch}}=2n_{\text{cell}}$) in the absence (presence) of the spin degree of freedom [49]. The Bloch Hamiltonians for the studied models are constructed in Supplementary Note XI), and made available as MATHEMATICA notebooks in the data repository [60].

We further consider the generation of density from HBT. Given a hyperbolic Bloch Hamiltonian, we perform random sampling of $N_{\mathbf{k}}$ momenta over the 4D hypercubic BZ, $\forall j \in \{1, 2, 3, 4\} : k_j \in [-\pi, \pi]$. The collected list of eigenvalues $\{\varepsilon_j\}_{j=1}^{N_{\mathbf{k}} D_{\text{Bloch}}}$ is converted into a continuous DoS function via

$$\rho^{\text{HBT}}(E) = \frac{1}{N_{\mathbf{k}} D_{\text{Bloch}}} \sum_{j=1}^{N_{\mathbf{k}} D_{\text{Bloch}}} f_{\eta}(E - \varepsilon_j) \quad (\text{S13})$$

where $f_{\eta}(\varepsilon) = \frac{1}{\eta\sqrt{2\pi}} \exp\left[-\frac{\varepsilon^2}{2\eta^2}\right]$ is a Gaussian smearing function. The factor in front of the summation symbol is chosen such that $\rho^{\text{HBT}}(E)$ integrates to 1. We use $\eta = 0.063$ and $N_{\mathbf{k}} = 2 \times 10^4$ throughout the manuscript.

V. Flake Hamiltonian in position space.

Two inputs are used to algorithmically construct the lattice Hamiltonian $\tilde{\mathcal{H}}^{\text{flake}}$ on a circular-flake in position space: the hyperbolic Bloch Hamiltonian $\mathcal{H}(\mathbf{k})$, and the target number \tilde{N}_{UC} of unit cells. The Bloch Hamiltonian has components $\mathcal{H}(\mathbf{k}) = \{h_{ab}(\mathbf{k})\}_{a,b=1}^{n_{\text{cell}}}$. For the models presented in this work, one finds that $h_{ab}(\mathbf{k}) = t_{ab} e^{i\mathbf{k}\cdot\boldsymbol{\varrho}_{ab}}$ with a unique value of the 4-component vector $\boldsymbol{\varrho}_{ab}$ and of the hopping amplitude t_{ab} for each $a, b \in \{1, \dots, n_{\text{cell}}\}$. (Note that here we treat t_{ab} as a single complex number for spinless models, and as a complex-valued 2×2 matrix for spinful models.) The algorithm, which is implemented in the data repository [60], proceeds in the following steps.

First, we invert Eq. (S11) to determine an estimated radius $R(\tilde{N}_{\text{UC}}) = [\tilde{N}_{\text{UC}}/(1 + \tilde{N}_{\text{UC}})]^{1/2}$ of a disk in the complex plane that contains \tilde{N}_{UC} Bolza cells. We center one of the Bolza cells at $z = 0$, and we use the known action ρ_{γ_j} of generators γ_j on the complex coordinates in \mathbb{D} [Eq. (45) in Ref. 13] to identify the centers of all cells of the $\{8, 8\}$ (Bolza) lattice that lie within the distance $R(\tilde{N}_{\text{UC}})$ from the origin. (Note that the centers of the Bolza cells do not coincide with any site of the $\{8, 3\}$ lattice.) This results in a *list of Bolza cells*, $L_{\text{cells}} = \{w_\ell\}_{\ell=1}^{N_{\text{UC}}}$; here, each w_ℓ is a sequence of generators and their inverses (a “word”) that translates $z = 0$ to $\rho_{w_\ell}(0) = z_j$ within the disk of radius R (i.e., $|z_j| < R$), and N_{UC} is the total number of selected Bolza cells. The words w_ℓ are elements of the hyperbolic translation group, and act on complex coordinates inside the Poincaré disk by ρ_{w_ℓ} , which is the corresponding composition of ρ_{γ_j} (and of their inverses). The word ‘ \emptyset ’ of length zero (which corresponds to the identity of the translation group) is always present in L_{cells} ; it encodes the Bolza cell centered at $z = 0$. We then apply L_{cells} to generate a *list of sites* of the $\{8, 3\}$ lattice, $\tilde{L}_{\text{sites}} = \{(w_\ell, a)\}$, where $1 \leq a \leq n_{\text{cell}}$ labels the individual sites within each Bolza cell $w_\ell \in L_{\text{cells}}$. The complex coordinates of the sites are obtained as $z_{(w_\ell, a)} = \rho_{w_\ell}(z_{(\emptyset, a)})$.

We next use the list \tilde{L}_{sites} and the amplitudes t_{ab} to construct the real-space Hamiltonian $\tilde{\mathcal{H}}^{\text{flake}}$. The Hamiltonian has $\tilde{n}_{\text{flake}} \times \tilde{n}_{\text{flake}}$ components, where $\tilde{n}_{\text{flake}} = n_{\text{cell}} N_{\text{UC}}$ is the length of list \tilde{L}_{sites} . Since the presently considered tight-binding Hamiltonians contain only NN and NNN terms, we run the following routine. For each pair (x, y) with $x = (w_\ell, a)$ and $y = (w_m, b)$ in \tilde{L}_{sites} , compute the distance $d(z_x, z_y)$. If the distance is equal to the NN distance $d_1^{\{8, 3\}}$ or to the NNN distance $d_2^{\{8, 3\}}$, we set $(\tilde{\mathcal{H}}^{\text{flake}})_{x,y} = t_{ab}$. In the very last step, we smooth the boundary of the system by identifying sites that have only a single NN. We drop the corresponding rows and columns of $\tilde{\mathcal{H}}^{\text{flake}}$, which results in the final Hamiltonian $\mathcal{H}^{\text{flake}}$ that has a slightly decreased number of components $n_{\text{flake}} \times n_{\text{flake}}$ (we similarly define the corresponding shortened list of sites L_{sites} of length n_{flake}). Note that for spinful models, the counted Hamiltonian components are 2×2 blocks, i.e., the actual Hamiltonian dimension is $D_{\text{flake}} = n_{\text{flake}}$ ($D_{\text{flake}} = 2n_{\text{flake}}$) for spinless (spinful) models.

VI. Considered system sizes in the flake geometry.

The assumed system size varies between the figures. We encode the size for each calculation with the triplet “SIZE = $(\tilde{N}_{UC}, N_{UC}, n_{flake})$ ” (where N_{UC} and n_{flake} are selected automatically by the the above-outlined algorithm upon inputting \tilde{N}_{UC}).

For the hH model, the sizes are set up as follows:

- Fig. 1(b,c) and Fig. 2(c): SIZE = (700, 761, 8496),
- Supplementary Fig. S2(a,c) and Supplementary Fig. S4(a): SIZE = (400, 409, 4520),
- Fig. 4(a) and Supplementary Fig. S7(b): SIZE = (500, 569, 6344 \mapsto 896),
- Fig. 4(b,c) and Supplementary Fig. S4(b,c): SIZE = (200, 169, 1864).

For the rhKM model, we chose the following sizes:

- Supplementary Fig. S2(a,d) and Supplementary Fig. S3: SIZE = (200, 169, 1864),
- Fig. 3(b) and Fig. 5: SIZE = (300, 297, 3304),
- Supplementary Fig. S7(b): SIZE = (500, 569, 6344 \mapsto 896).

Note that in the calculations leading to Fig. 4(a) and to Supplementary Fig. S7(a,b), an additional level of removing sites at the boundary is applied, namely, starting with the list \tilde{L}_{sites} , we remove all sites with less than three nearest neighbors. Thus, instead of arriving at a system with 6344 sites, we obtain a much smaller system with 896 sites, cf. Supplementary Note XIII.

VII. Bulk density of states and integrated boundary density of states for the flake Hamiltonian.

Given a lattice Hamiltonian $\mathcal{H}^{\text{flake}}$ on a circular flake, we perform ED to find its eigensystem $\Lambda^{\text{flake}} = \{(E_j, |\phi_j\rangle)\}_{j=1}^{D_{\text{flake}}}$, where $|\phi_j\rangle$ is an eigenvector with eigenvalue E_j . Each eigenstate is a list of amplitudes, namely $|\phi_j\rangle = \{\phi_{j,x}\}_{x \in L_{\text{sites}}}$ for spinless models ($|\phi_j\rangle = \{\phi_{j,x,\sigma}\}_{x \in L_{\text{sites}}, \sigma \in \{\uparrow, \downarrow\}}$ for spinful models). For each state we define the *bulk weight* ϖ_j^{bulk} as the probability that the particle in such a state is located on the innermost unit cell (i.e., sites with $w_\ell = \emptyset$),

$$\varpi_j^{\text{bulk}} = \sum_{a=1}^{16} |\phi_{j,(\emptyset,a)}|^2 \quad \text{and} \quad \varpi_j^{\text{bulk}} = \sum_{a=1}^{16} \sum_{\sigma \in \{\uparrow, \downarrow\}} |\phi_{j,(\emptyset,a),\sigma}|^2 \quad (\text{S14})$$

for spinless and spinful models, respectively. We then convert the information about the eigenvalues and eigenvectors into a continuous DoS function via

$$\rho_{\text{bulk}}^{\text{ED}}(E) = \frac{1}{D_{\text{Bloch}}} \sum_{j=1}^{D_{\text{flake}}} \varpi_j^{\text{bulk}} f_\eta(E - E_j) \quad (\text{S15})$$

with the smearing function f_η defined below Eq. (S13). The prefactor $1/D_{\text{Bloch}}$ guarantees that $\rho_{\text{bulk}}^{\text{ED}}(E)$ integrates to 1. To achieve a simple comparison with the HBT data, we use $\eta = 0.063$ throughout the manuscript.

We next define the integrated DoS at the boundary in analogy with Eq. (S15), where the only difference is the replacement $\varpi_j^{\text{bulk}} \mapsto \varpi_j^{\text{bound.}}$, with

$$\varpi_j^{\text{bound.}} = \sum_{x \in L_{\text{bound.}}} |\phi_{j,x}|^2 \quad \text{and} \quad \varpi_j^{\text{bound.}} = \sum_{x \in L_{\text{bound.}}} \sum_{\sigma \in \{\uparrow, \downarrow\}} |\phi_{j,x,\sigma}|^2 \quad (\text{S16})$$

for spinless and spinful models, respectively, where $L_{\text{bound.}}$ is a sublist of L_{sites} that selects sites with two nearest neighbors.

VIII. Real-space invariants.

For the energy gap at chemical potential μ , we compute the *real-space Chern number* using the formula from Ref. 39,

$$\mathcal{C}_{\text{RS}}(\mu) = 12\pi i \sum_{j \in A} \sum_{k \in B} \sum_{\ell \in C} \left(\mathbb{P}_{jk}^{\mu} \mathbb{P}_{k\ell}^{\mu} \mathbb{P}_{\ell j}^{\mu} - \mathbb{P}_{j\ell}^{\mu} \mathbb{P}_{\ell k}^{\mu} \mathbb{P}_{kj}^{\mu} \right) \quad (\text{S17})$$

where \mathbb{P}^{μ} is the projector onto the subspace of occupied single-particle states at chemical potential μ , and A, B, C are three regions in the bulk of the systems that (i) do not extend all the way to the boundary, and which (ii) are arranged counter-clockwise around the center of the system [cf. Fig. S2(b)].

In the presence of time-reversal symmetry, we compute the *real-space spin Chern number* ν_{RS} following the ideas of Refs. 41 and 42. Namely, we first construct the *projected spin operator* $\mathbb{P}_z^{\mu} = \mathbb{P}^{\mu} \sigma_z \mathbb{P}^{\mu}$. Next, we perform spectral decomposition of the projected spin operator into eigenstates ($|\zeta_j\rangle$) and eigenvalues (S_j). As long as the spin-mixing Rashba term is weak, the eigenvalues S_j remain close to ± 1 , allowing us to define the index sets \mathfrak{S}_{\pm} ; in addition, there are unphysical zero eigenvalues, which correspond to the part of the Hilbert space that is projected out by \mathbb{P}^{μ} . This allows us to define projectors $\mathbb{P}_{\pm} = \sum_{j \in \mathfrak{S}_{\pm}} |\zeta_j\rangle \langle \zeta_j|$. The integer-valued real-space spin Chern number is then obtained as

$$\nu_{\text{RS}}(\mu) = \frac{1}{2} [\nu_{\text{RS}}^+(\mu) - \nu_{\text{RS}}^-(\mu)], \quad (\text{S18})$$

where $\nu_{\text{RS}}^{\pm}(\mu)$ are computed per Eq. (S17) with replaced $\mathbb{P}^{\mu} \mapsto \mathbb{P}_{\pm}^{\mu}$. Note that for strong SOC, the eigenstates of \mathbb{P}_z no longer exhibit a clear spectral gap between the two sets \mathfrak{S}_{\pm} , and the formula in Eq. (S18) ceases to be applicable. We verified that this issue does not arise for our selected model parameters.

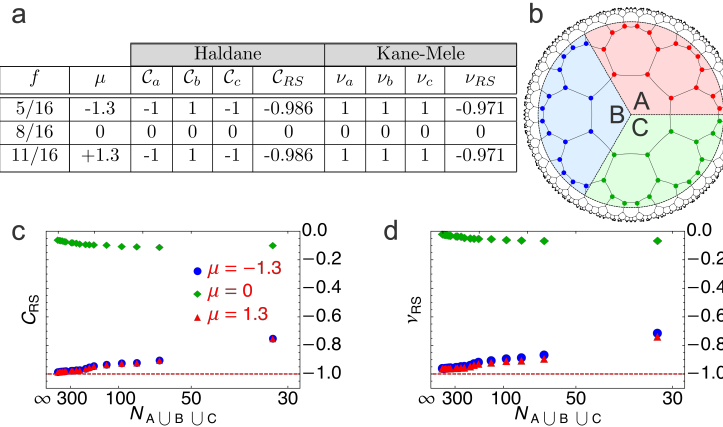


FIG. S2. **Topological invariants.** **a.** Summary of topological invariants for the hyperbolic Haldane and reduced hyperbolic KM models for their respective three energy gaps, labelled by filling fraction f and chemical potential μ . We show both momentum-space band invariants (subscripts a and b) and real-space topological markers (subscript RS). **b.** Regions A, B, C involved in the computation of the real-space invariants. **c, d.** Convergence of the computed real-space Chern number (c) and real-space spin Chern number (d) for the three energy gaps (labelled by μ) upon increasing the size of the regions A, B, C. Here $N_{A \cup B \cup C}$ is the total number of sites in the three regions.

Haldane/ Kane-Mele										
$N_{A \cup B \cup C}$	16	32	64	80	96	120	152	168	184	216
\mathcal{C}_{RS} ($\mu = \pm 1.3$)	-0.661	-0.751	-0.904	-0.921	-0.924	-0.934	-0.944	-0.953	-0.962	-0.972
ν_{RS} ($\mu = -1.3$)	-0.638	-0.723	-0.876	-0.895	-0.903	-0.916	-0.926	-0.937	-0.948	-0.955
ν_{RS} ($\mu = +1.3$)	-0.654	-0.747	-0.902	-0.915	-0.918	-0.929	-0.937	-0.945	-0.955	-0.964
$N_{A \cup B \cup C}$	240	272	288	368	400	448	496	544	624	
\mathcal{C}_{RS} ($\mu = \pm 1.3$)	-0.973	-0.976	-0.976	-0.979	-0.980	-0.981	-0.982	-0.984	-0.986	
ν_{RS} ($\mu = -1.3$)	-0.957	-0.963	-0.963	-0.966	-0.966	-0.968	-0.969	-0.971	-0.970	
ν_{RS} ($\mu = +1.3$)	-0.965	-0.967	-0.968	-0.969	-0.969	-0.970	-0.971	-0.971	-0.970	

TABLE S2. **Tabulated values of data in Fig. S2(c,d).** The values indicate the convergence of the topological markers in positions space to values ± 1 as the number of sites $N_{A \cup B \cup C}$ in the summation region is increased.

[4]

IX. Gaussian projector operator.

Given the eigensystem of a flake Hamiltonian, $\Lambda^{\text{flake}} = \{(E_j, |\phi_j\rangle)\}_{j=1}^{D_{\text{flake}}}$, we construct for an energy range $[\mu - \sigma, \mu + \sigma]$ within a topological energy gap the operator

$$\mathbb{P}_{(\mu, \sigma)} = \sum_{j=1}^{D_{\text{flake}}} \exp \left[-\frac{(E_j - \mu)^2}{2\sigma^2} \right] |\phi_j\rangle\langle\phi_j|. \quad (\text{S19})$$

Note that $\mathbb{P}_{(\mu, \sigma)}$ is not a projector in the traditional sense, since its eigenvalues are arbitrary numbers in range $[0, 1]$. The idea behind the exponential weight factor in Eq. (S19) is that, per the approximately linear dispersion of the edge state visible in Fig. 4(a), we construct a Gaussian function in angular momentum ℓ . Therefore, the wave function $\mathbb{P}_{(\mu, \sigma)} |\varphi_{\text{site}}\rangle$ has approximately Gaussian coefficients in its decomposition to angular momenta, implying it constitutes a Gaussian wave packet in the angular coordinate α .

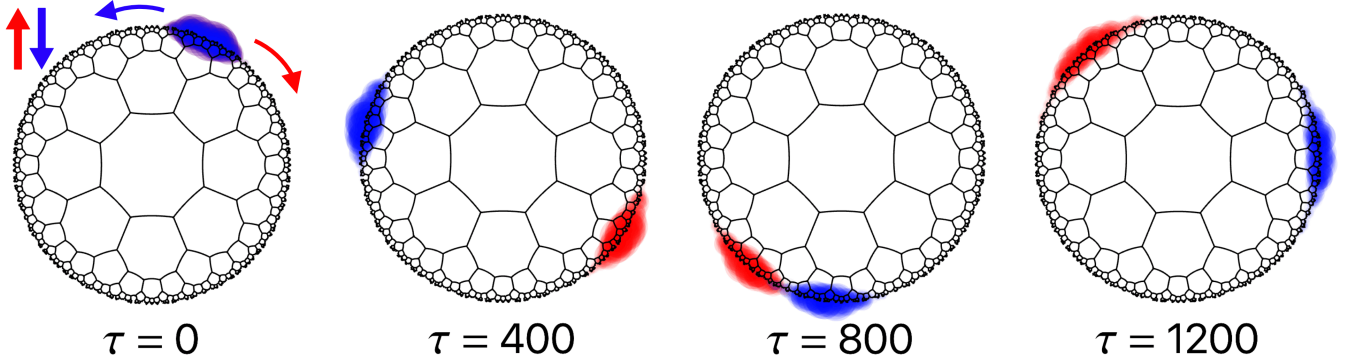


FIG. S3. **Propagation of edge states in the rhKM model.** We compute and plot the propagation of helical edge states around the boundary of a flake supporting the rhKM model. The time evolution is computed according to the description in section ‘*Bulk-boundary correspondence*’ of the main text, and we use the Gaussian projector $\mathbb{P}_{(\mu, \sigma)}$ with $(\mu, \sigma) = (1.3, 0.025)$. The indicated time τ is counted in multiples of $1/t_1$. The initial single-site localized state $|\varphi_{\text{site}}\rangle$ was chosen to have the form $\frac{1}{\sqrt{2}}(1, 1)^\top$ in the spin degree of freedom. We observe that time-evolution splits $\mathbb{P}_{(\mu, \sigma)} |\varphi_{\text{site}}\rangle$ into a pair of counter-propagating wave packets that during the time evolution pass through one another without scattering.

X. Models of disorder.

For the hH Hamiltonian $\mathcal{H}_{\text{hH}}^{\text{flake}}$, we consider the addition of random on-site potential, i.e., for each site a we add to $(\mathcal{H}_{\text{hH}}^{\text{flake}})_{aa}$ a random value drawn from the box distribution bounded by $\pm W_{\max}$.

For the rhKM Hamiltonian $\mathcal{H}_{\text{rhKM}}^{\text{flake}}$, we consider the addition of a random spin-dependent term to each pair (a, b) of NN and NNN sites. We specifically consider terms that are off-diagonal in the spin-degree of freedom; namely, for each pair (a, b) we draw random values $\alpha_{x,y} \in [-W_{\max}, +W_{\max}]$, and increase the 2×2 Hamiltonian blocks as follows:

$$\text{TR-symmetric disorder : } (\mathcal{H}_{\text{rhKM}}^{\text{flake}})_{ab} = i(\alpha_x \sigma_x + \alpha_y \sigma_y), \quad (\text{S20})$$

$$\text{TR-breaking disorder : } (\mathcal{H}_{\text{rhKM}}^{\text{flake}})_{ab} = (\alpha_x \sigma_x + \alpha_y \sigma_y), \quad (\text{S21})$$

with $(\mathcal{H}_{\text{rhKM}}^{\text{flake}})_{ba} = (\mathcal{H}_{\text{rhKM}}^{\text{flake}})_{ab}^\dagger$ for both cases. The disorder in Eq. (S20) is interpretable as random Rashba SOC, while the one in Eq. (S21) corresponds to random in-plane magnetic fields along the trajectory connecting sites (a, b) .

The localization of a normalized eigenstate $|\phi_j\rangle$ is quantified by the inverse participation ratio, defined for spinless and spinful systems as

$$\text{IPR}_j = \sum_{a=1}^{n_{\text{flake}}} |\phi_{j,a}|^4 \quad \text{resp.} \quad \text{IPR}_j = \sum_{a=1}^{n_{\text{flake}}} (|\phi_{j,a,\uparrow}|^2 + |\phi_{j,a,\downarrow}|^2)^2. \quad (\text{S22})$$

One easily verifies that if $|\phi_j\rangle$ were homogeneously distributed over N sites, then $\text{IPR}_j = 1/N$. This implies the interpretation that an eigenstate characterized by IPR_j as being distributed over approximately $1/\text{IPR}_j$ sites.

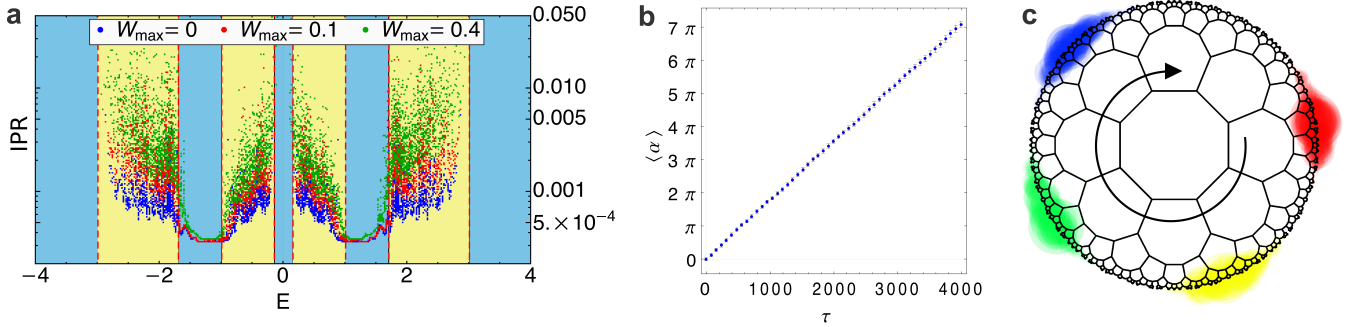


FIG. S4. Robustness against Anderson disorder in the hyperbolic Haldane model. The disorder chosen for the hyperbolic Haldane model corresponds to the addition of a random on-site potential drawn from a box distribution in range $[-W_{\max}, W_{\max}]$. **a**, IPR of the individual eigenstates for various choices of disorder strength W_{\max} . Note that the domain of low values of IPR has reduced to a narrower range of energies for the green data ($W_{\max} = 0.4$), indicating the shrinking of the bulk energy gap; nevertheless, the robustness of edge states with low IPR is manifest. **b–c**, Propagation of chiral edge states in disordered hH model. The calculation is analogous to Fig. 4(b,c) of the main text, but here we assume the addition of a strong random on-site potential with disorder strength $W_{\max} = 0.4$ (green in panel **a**). The wave packet continues to propagate around the flake boundary with nearly uniform angular velocity. The parameters of the Gaussian projector are $(\mu, \sigma) = (1.3, 0.025)$, and the data in red/yellow/green/blue color consecutively correspond to the wave packet at times $\tau = (0, 240, 480, 720)$, $(\mu, \sigma) = (1.3, 0.025)$.

XI. Hyperbolic Bloch Hamiltonians of the studied models

Since the hyperbolic Bloch Hamiltonians $\mathcal{H}(\mathbf{k})$ studied in this work are 16×16 and 32×32 matrices, we do not write them explicitly. Instead, we include here the MATHEMATICA code that generates these Hamiltonians when compiled (the corresponding MATHEMATICA notebooks are included in the data repository [60]).

We first specify the following:

```
$Assumptions = {
  k1 \[Element] Reals, k2 \[Element] Reals,
  k3 \[Element] Reals, k4 \[Element] Reals,
  t1 \[Element] Reals, t2 \[Element] Reals,
  flux \[Element] Reals, M \[Element] Reals, LR \[Element] Reals
};

kList = {k1, k2, k3, k4, -k1, -k2, -k3, -k4};
```

The hyperbolic Bloch Hamiltonian of the NN model on the $\{8, 3\}$ lattice is obtained as `Hnn` with the following code:

```
Hnn = ConstantArray[0, {16, 16}];

For[a = 1, a < 9, a++,
  Hnn[[Mod[a, 8] + 1, a]] = t1;
  Hnn[[a + 8, a]] = t1;
  Hnn[[8 + Mod[a + 4, 8] + 1, 8 + a]] = t1*Exp[-I*kList[[a]]];
];

Hnn = FullSimplify[Hnn + ConjugateTranspose[Hnn]];
```

After including the mass term, we obtain the hyperbolic Bloch Hamiltonian $\mathcal{H}_{\{8,3\}}(\mathbf{k})$ as `H83` with the following code:

```
Hmass = ConstantArray[0, {16, 16}];
For[a = 1, a < 9, a++,
  Hmass[[a, a]] += M*Power[-1, a + 1];
  Hmass[[a + 8, a + 8]] += -M*Power[-1, a + 1];
];

H83 = Hnn + Hmass;
```

To obtain the hyperbolic Bloch Hamiltonian $\mathcal{H}_{\text{hH}}(\mathbf{k})$ for the hyperbolic Haldane model, encoded as `Hh` in the code below, we further define a matrix `Hflux` of NNN terms.

```
Hflux = ConstantArray[0, {16, 16}];

For[a = 1, a < 9, a++,
  Hflux[[Mod[a + 1, 8] + 1, a]] = t2*f;
  Hflux[[a, 8 + Mod[a, 8] + 1]] = t2*f;
  Hflux[[8 + Mod[a - 2, 8] + 1, a]] = t2*f;

  Hflux[[8 + Mod[a + 4, 8] + 1, a]] = t2*f*Exp[-I*kList[[a]]];
  Hflux[[a, 8 + Mod[a + 2, 8] + 1]] =
    t2*f*Exp[I*kList[[Mod[a - 2, 8] + 1]]];

  Hflux[[8 + Mod[a + 2, 8] + 1, 8 + Mod[a + 4, 8] + 1]] =
    t2*f*Exp[I*(kList[[a]] - kList[[Mod[a - 2, 8] + 1]])];
];

Hflux = FullSimplify[Hflux + ConjugateTranspose[Hflux]];

Hh = FullSimplify[H83 + Hflux /. f \[Rule] Exp[I*flux]];
```

We next proceed to construct the hyperbolic Bloch Hamiltonian $\mathcal{H}_{\text{rhKM}}(\mathbf{k})$ of the reduced hyperbolic Kane-Mele model. To that end, we first double the Haldane model into a ‘quantum spin Hall’ Hamiltonian Hqsh :

```
Hqsh = ArrayFlatten[
  {
    {((H83 + Hflux) /. f \[Rule] Exp[I*flux]), 0},
    {0, ((H83 + Hflux) /. f \[Rule] Exp[\[Minus]I*flux])}
  }
];
```

The spin-orbit-coupled rhKM model is finally obtained as Hhkm with the following code:

```
Hsoc = ConstantArray[0, {16, 16}];

For[a = 1, a < 9, a++,
  alpha = -Pi/2 - (a - 1)*(2 Pi/8);
  Hsoc[[Mod[a, 8] + 1, a]] = I*(Cos[alpha]*PauliMatrix[1] + Sin[alpha]*PauliMatrix[2]);
  Hsoc[[a, Mod[a, 8] + 1]] = -I*(Cos[alpha]*PauliMatrix[1] + Sin[alpha]*PauliMatrix[2]);

  beta = Pi/8 - (a - 1)*(2 Pi/8);
  Hsoc[[a + 8, a]] = I*(Cos[beta]*PauliMatrix[1] + Sin[beta]*PauliMatrix[2]);
  Hsoc[[a, a + 8]] = -I*(Cos[beta]*PauliMatrix[1] + Sin[beta]*PauliMatrix[2]);

  gamma = 0 - (a - 1)*(2 Pi/8);
  Hsoc[[8 + Mod[a + 4, 8] + 1, 8 + a]] =
    I*(Cos[gamma]*PauliMatrix[1] + Sin[gamma]*PauliMatrix[2])*Exp[-I*kList[[a]]];
  Hsoc[[8 + a, 8 + Mod[a + 4, 8] + 1]] =
    -I*(Cos[gamma]*PauliMatrix[1] + Sin[gamma]*PauliMatrix[2])*Exp[I*kList[[a]]];
];

For[a = 1, a < 17, a++,
  For[b = 1, b < 17, b++,
    If[Hsoc[[a, b]] == 0,
      Hsoc[[a, b]] = ConstantArray[0, {2, 2}];
    ];
  ];
];

Hsoc = ArrayFlatten@Transpose[Hsoc, {3, 4, 1, 2}];
Hhkm = (Hqsh /. flux \[Rule] Pi/2) + LR*Hsoc;
```

XII. Wilson-loop extraction of topological band invariants

We extract topological band invariants of hyperbolic Bloch Hamiltonians on two-dimensional planes in the 4D BZ using the Wilson-loop technique [50, 51]. The utilized code is shared in the data repository [60].

First, we determine the Chern numbers $\mathcal{C}_a, \mathcal{C}_b, \mathcal{C}_c \in \mathbb{Z}$ of the hyperbolic Haldane model $\mathcal{H}_{\text{hH}}(\mathbf{k})$ by computing the Wilson loop in the k_2 -, k_3 - resp. k_4 -direction (labelled as W_2 , W_3 , resp. W_4) as a function of k_1 . The results of our analysis are shown in Fig. S5, and tabulated in Fig. S2(a).

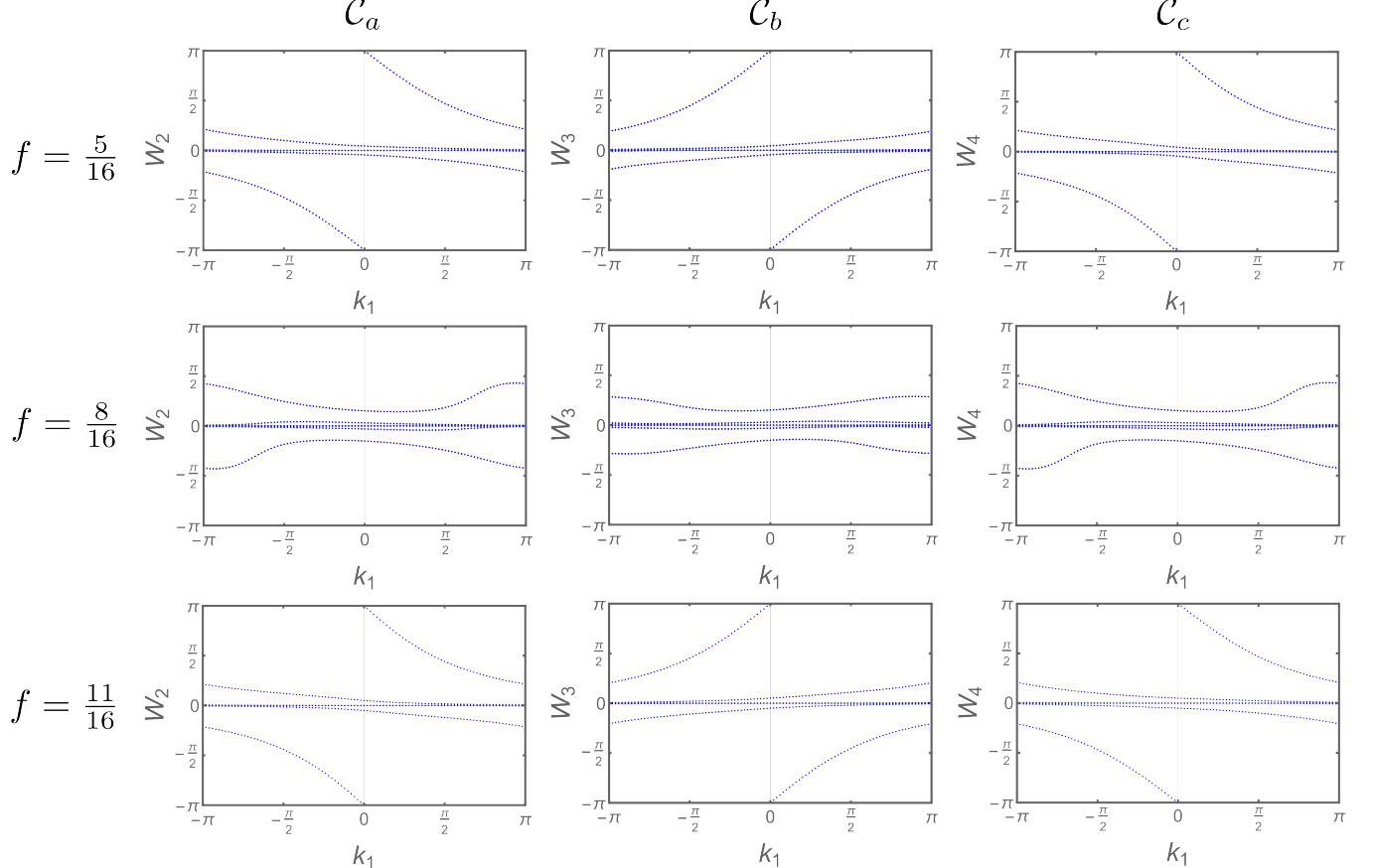


FIG. S5. **Wilson-loop spectra for the hH model.** Rows represent the three energy gaps of the model at the indicated filling fractions f , while columns correspond to the three pairs of planes that we do not relate by symmetry in the discussion in the main text. The Wilson spectra reveal the values of the Chern numbers tabulated in Fig. S2(a). Note that the number of plotted Wilson bands matches the number of filled energy bands (numerators of f); however, some of the bands are not resolved since they coincide close to zero value.

We next determine the Kane-Mele invariants $\nu_a, \nu_b, \nu_c \in \mathbb{Z}_2$ for the reduced hyperbolic Kane-Mele model $\mathcal{H}_{\text{rhKM}}(\mathbf{k})$ by computing the Wilson loop in the k_2 -, k_3 - resp. k_4 -direction (labelled again as W_2, W_3 , resp. W_4) as a function of k_1 . The results of our analysis are shown in Fig. S6.

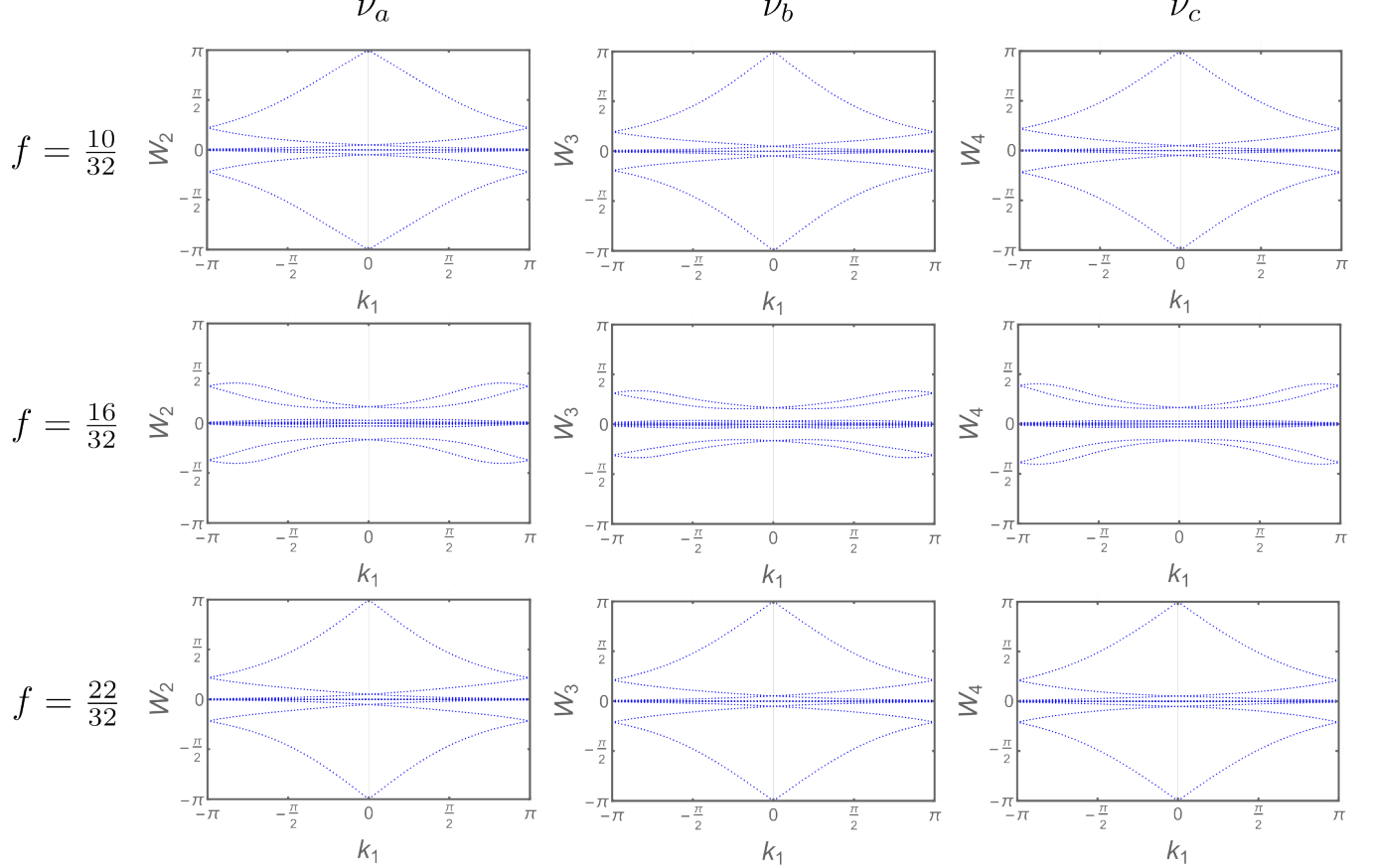


FIG. S6. Wilson-loop spectra for the rhKM model. Rows represent the three energy gaps of the model at the indicated filling fractions f , while columns correspond to the three pairs of planes that we do not relate by symmetry in the discussion in the main text. The Wilson spectra reveal the values of the Kane-Mele invariants tabulated in Fig. S2(a). The number of plotted Wilson bands matches the number of filled energy bands (numerators of f); however, some of the bands are not resolved since they coincide close to zero value.

XIII. Extraction of the edge mode dispersion

In this supplementary note we describe a method we developed to determine the angular momentum of a given eigenstate of the Hamiltonian defined on a hyperbolic lattice. This method is used to generate the data for the dispersion of the chiral edge state of the hH model plotted in Fig. 4a of the main text.

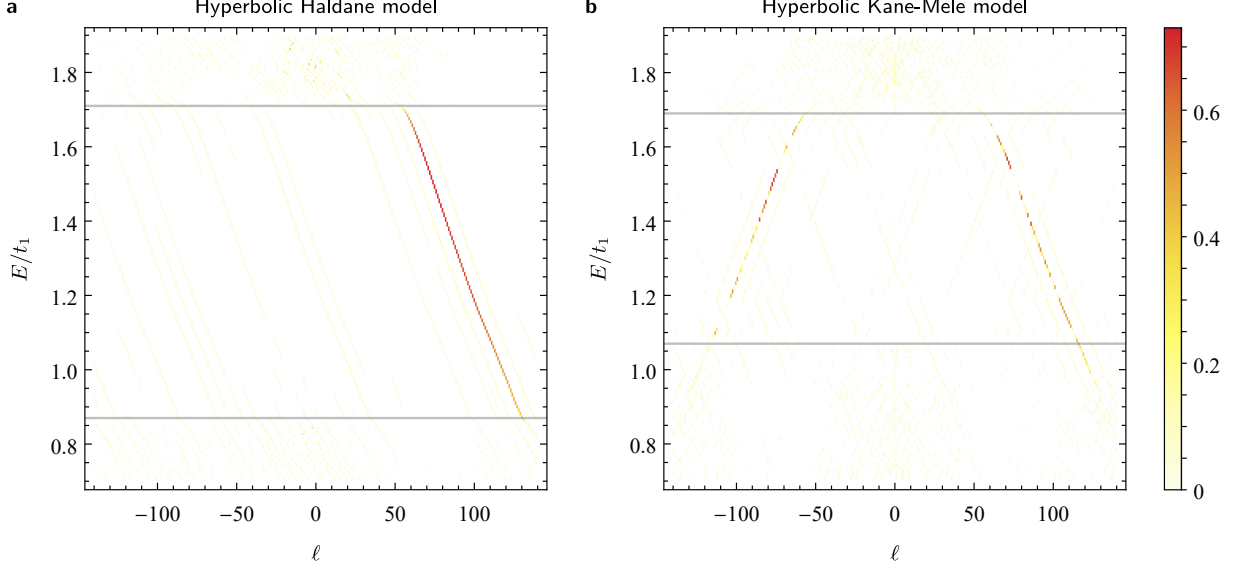


FIG. S7. Angular momentum dispersion of edge modes. Contribution ϕ_ℓ [cf. Eq. (S39) in Supplementary Note XIII] of different angular momenta to the states lying in the upper energy gap for **a**, the Haldane model, and **b**, the reduced Kane-Mele model defined on the flake of the $\{8, 3\}$ lattice shown in Supplementary Fig. S9. The horizontal grey lines indicate the band edges below and above the gap, and were determined from the density of states $\rho_{\text{bulk}}^{\text{ED}}$ for the here considered system size. **a**, In the Haldane model, there is a single (chiral) propagating edge mode with a very sharp angular momentum dispersion lying exactly in the gap. **b**, In the case of the Kane-Mele model, we find in the gap two (helical) counter-propagating edge modes. The two edge-state branches are characterized by opposite sign of the angular momentum (ℓ) as well as of the angular momentum dispersion ($dE/d\ell$).

The method relies on a decomposition of functions defined on the disk $\mathbb{D}_R = \{z \in \mathbb{C} \mid |z| \leq R\}$ of radius $0 < R < 1$ with the hyperbolic metric given by Eq. (S1) into eigenmodes of the Laplace-Beltrami operator

$$\Delta = \left(1 - |z|^2\right)^2 \left(\frac{\partial^2}{\partial x^2} + \frac{\partial^2}{\partial y^2}\right), \quad (\text{S23})$$

where $z = x + iy \in \mathbb{C}$. The solutions to the Dirichlet problem

$$(\Delta + \lambda)u(z) = 0, \quad u(z)|_{(z) \in \partial\mathbb{D}_R} = 0 \quad (\text{S24})$$

form an orthonormal basis for functions on \mathbb{D}_R and they are given [6, 13] by

$$u_{n,\ell}(z) = \frac{g_{k_n,\ell}(|z|)}{\|g_{k_n,\ell}\|} e^{i\ell \arg(z)}, \quad (\text{S25})$$

where

$$g_{k,\ell}(r) = \begin{cases} P_{\frac{1}{2}(-1+ik)}^0 \left(\frac{1+r^2}{1-r^2}\right), & \ell = 0 \\ \left(\prod_{m=0}^{\ell-1} \left(-\frac{1}{2} - m + ik\right)\right)^{-1} P_{\frac{1}{2}(-1+ik)}^\ell \left(\frac{1+r^2}{1-r^2}\right), & \ell > 0 \\ (-1)^\ell g_{k,|\ell|}(r), & \ell < 0 \end{cases} \quad (\text{S26})$$

$P_q^\ell(s)$ are the associated Legendre functions, $\|g\| = \sqrt{\langle g, g \rangle}$ is the norm induced by the inner product on \mathbb{D}_R

$$\langle v, w \rangle = \int_{|z| \leq R} \frac{d^2 z}{(1 - |z|^2)^2} v(z)^* w(z), \quad (\text{S27})$$

$k_{n,\ell}$ is the n -th zero of

$$k \mapsto P_{\frac{1}{2}(-1+ik)}^\ell \left(\frac{1+R^2}{1-R^2} \right), \quad (\text{S28})$$

and $\ell \in \mathbb{Z}$. The solutions to Eq. (S28) correspond to zeroes of $g_{k,\ell}(R)$, cf. Supplementary Fig. S8a.

For the flake of the $\{8, 3\}$ lattice shown in Supplementary Fig. S9 that we define our models on, all the eigenvalues $\lambda_{n,\ell}$ are shown in Supplementary Fig. S8b as functions of n and ℓ and the five solutions to Eq. (S24) with smallest $\lambda_{n,\ell}$ are plotted in the top row of Supplementary Fig. S10.

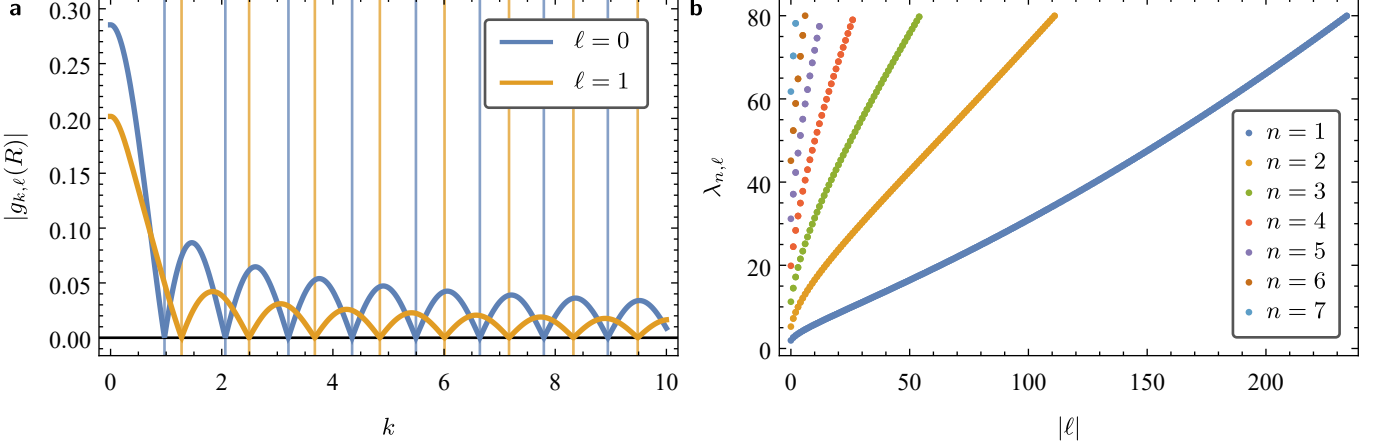


FIG. S8. **Eigenvalues of the Laplace-Beltrami operator.** Illustration of how to find $k_{n,\ell}$ and the resulting eigenvalues $\lambda_{n,\ell}$ with 896 sites of the $\{8, 3\}$ lattice shown in Fig. S9a. **a**, The function $k \mapsto g_{k,\ell}(R)$ for $\ell = 0$ (blue) and $\ell = 1$ (orange) and with $R = 0.991437$ chosen as illustrated in Fig. S9b. The first few zeroes $k_{n,\ell}$ are marked by vertical lines. **b**, The first 896 eigenvalues $\lambda_{n,\ell}$ as a function of $|\ell|$ with the different branches corresponding to different n .

A function $v(z)$ on \mathbb{D}_R can then be decomposed into the eigenfunctions $u_{n,\ell}(z)$:

$$v(z) = \sum_{n>0} \sum_{\ell \in \mathbb{Z}} v_{n,\ell} u_{n,\ell}(z), \quad (\text{S29a})$$

$$v_{n\ell} = \langle u_{n,\ell}, v \rangle = \int_{|z| \leq R} \frac{d^2 z}{(1 - |z|^2)^2} u_{n,\ell}(z)^* v(z). \quad (\text{S29b})$$

In Eq. (S25) we recognize that ℓ can be interpreted as angular momentum. If $v(z)$ is normalizable, $\|v\| < \infty$,

$$v_\ell = \sum_{n>0} |v_{n,\ell}|^2 \quad (\text{S30})$$

gives the contributions of different values of angular momentum ℓ to the function $v(z)$.

This can be used to find the contributions of angular momenta to quantities (vectors) defined on the lattice, e.g., the eigenstates of the Hamiltonian $\mathcal{H}_{\{8,3\}}^{\text{flake}}$ defined on a flake of the $\{8, 3\}$ lattice. A normalized vector $|\phi\rangle = (\phi_1, \dots, \phi_N)^\top$ defined on the lattice given by the finite set of sites $\{z_i\}_{i=1}^N$ induces the following function on \mathbb{D}_R

$$\phi^{(\alpha)}(z) = \sum_{i=1}^N \phi_i \eta_i^{(\alpha)}(z), \quad (\text{S31})$$

where $\eta_i(z)$ is non-vanishing only in the Wigner-Seitz cell of the lattice site i (the Wigner-Seitz cell is defined as the region of \mathbb{D}_R that has shorter hyperbolic distance to site i than to any other site of the flake), and satisfies

$$\int_{|z| \leq R} \frac{d^2 z}{(1 - |z|^2)^2} |\eta_i^{(\alpha)}(z)|^2 = 1. \quad (\text{S32})$$

Various choices for $\eta_i(z)$ are possible. Here we consider two options:

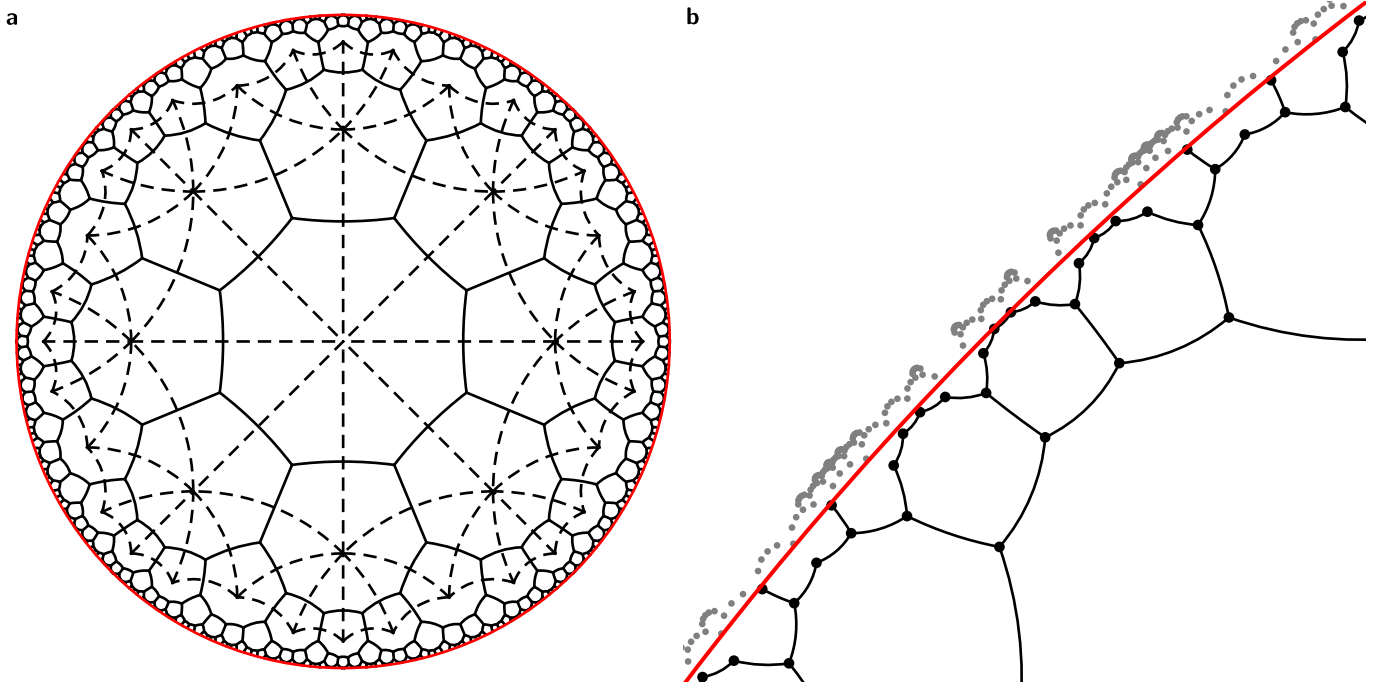


FIG. S9. Flake of the $\{8,3\}$ lattice used to extract the edge mode dispersion. **a,** The flake with 896 sites with nearest-neighbour bonds (black lines). Some of the Wigner-Seitz unit cells are indicated by black dashed lines. The red circle bounds the disk of radius R which determines the Dirichlet boundary conditions for $u(z)$. **b,** The radius R is defined as the maximal radius r such that additional sites of the infinite hyperbolic lattice (gray points) not included in the flake (whose sites are shown with black points) lie outside the disk \mathbb{D}_r .

Option (1): $\eta_i^{(1)}(z) = \Theta_i(z)/\sqrt{A_{\text{WS}}}$, and

Option (2): $\eta_i^{(2)}(z) = \sqrt{A_{\text{WS}}}(1 - |z_i|^2)^2 \delta^{(2)}(z - z_i)$.

In both of the above, A_{WS} is the (hyperbolic) area of a Wigner-Seitz unit cell (cf. Fig. S9); and $\Theta_i(z)$ in the first expression is a “region function” that is equal to one inside (and to zero outside) the Wigner-Seitz cell of site i . For both of the above options,

$$\langle \eta_i^{(\alpha)}, \phi^{(\alpha)} \rangle = \sum_j \phi_j \int_{|z| \leq R} \frac{d^2 z}{(1 - |z|^2)^2} [\eta_i^{(\alpha)}(z)]^* \eta_j^{(\alpha)}(z) = \phi_i \quad (\text{S33})$$

allows us get back the i^{th} component of vector $|\phi\rangle$.

The extension $\phi^{(\alpha)}(z)$ of $|\phi\rangle$ to the full disk \mathbb{D}_R allows us to apply the decomposition into eigenmodes of the Laplace-Beltrami operator given in Eq. (S29) to the vector $|\phi\rangle$:

$$\phi_{n,\ell}^{(\alpha)} = \langle u_{n,\ell}, \phi^{(\alpha)} \rangle = \sum_i \phi_i \langle u_{n,\ell}, \eta_i^{(\alpha)} \rangle. \quad (\text{S34})$$

For choice (1) this becomes

$$\phi_{n,\ell}^{(1)} = \sqrt{A_{\text{WS}}} \sum_i \phi_i \overline{u_{n,\ell}}(z_i)^* \quad (\text{S35})$$

where $\overline{u_{n,\ell}}(z_i)$ is the average over the i^{th} Wigner-Seitz cell WS_i :

$$\overline{u_{n,\ell}}(z_i) = \int_{z \in \text{WS}_i} \int_{|z| \leq R} \frac{d^2 z}{(1 - |z|^2)^2} u_{n,\ell}(z). \quad (\text{S36})$$

Choice (2) results in a much simpler expression only involving $u_{n,\ell}(z)$ evaluated at the lattice sites:

$$\phi_{n,\ell}^{(2)} = \sqrt{A_{\text{WS}}} \sum_i \phi_i u_{n,\ell}(z_i)^*. \quad (\text{S37})$$

For the two choices we define

- (1): $|\psi_{n,\ell}^{(1)}\rangle = \sqrt{A_{\text{WS}}}(\overline{u_{n,\ell}}(z_1), \dots, \overline{u_{n,\ell}}(z_N))^{\top}$, resp.
- (2): $|\psi_{n,\ell}^{(2)}\rangle = \sqrt{A_{\text{WS}}}(u_{n,\ell}(z_1), \dots, u_{n,\ell}(z_N))^{\top}$,

allowing us to express the coefficients $\phi_{n,\ell}$ compactly as

$$\phi_{n,\ell}^{(\alpha)} = \langle \psi_{n,\ell}^{(\alpha)} | \phi \rangle. \quad (\text{S38})$$

Some examples of $|\psi_{n,\ell}^{(1)}\rangle$ are shown in the bottom row of the Supplementary Fig. S10. Finally, we define the angular-momentum components

$$\phi_{\ell}^{(\alpha)} = \sum_{n>0} |\phi_{n,\ell}^{(\alpha)}|^2. \quad (\text{S39})$$

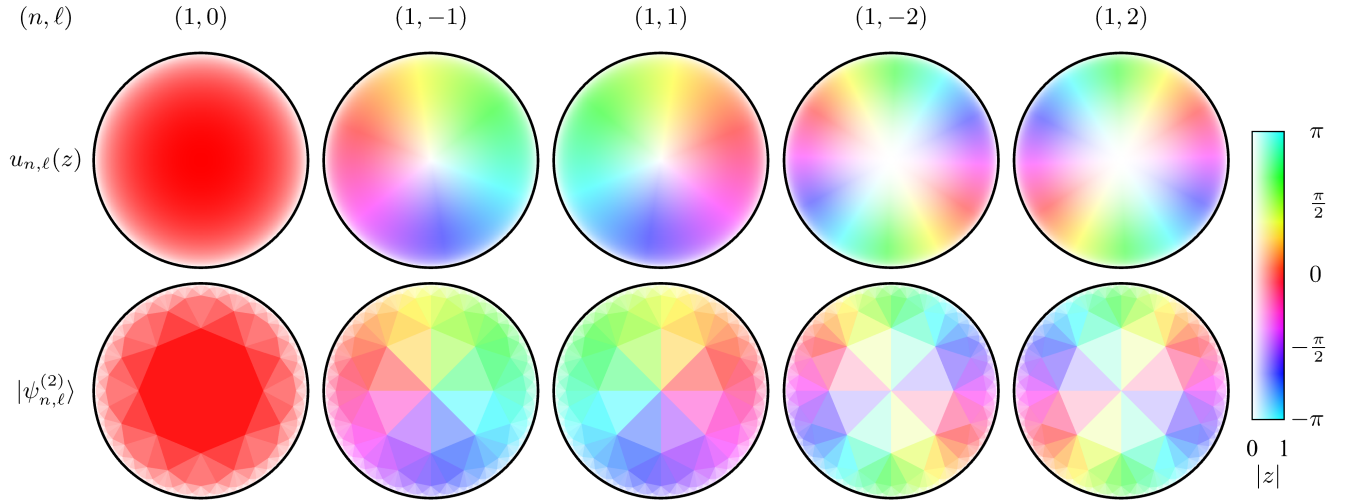


FIG. S10. **Eigenmodes of the Laplace-Beltrami operator.** Examples of eigenmodes $u_{n,\ell}(z)$ (top row) of the Laplace-Beltrami operator with Dirichlet boundary conditions for $|z| = R = 0.991437$. The bottom row shows the discretized versions $|\psi_{n,\ell}^{(2)}\rangle$, i.e., $u_{n,\ell}$ evaluated at the lattice sites of the flake shown in Supplementary Fig. S9. In both rows the absolute value is encoded in the intensity and the argument in the color (see legend). The header gives the quantum numbers (n, ℓ) for each eigenmode.

Note that the discretized approximations $|\psi_{n,\ell}^{(\alpha)}\rangle$ of the Laplace-Beltrami eigenmodes $u_{n,\ell}(z)$ are *neither orthogonal nor normalized*, and therefore subsets with N elements generally do not form a basis of \mathbb{C}^N . In general, a large number of $|\psi_{n,\ell}\rangle$ are required to characterize an arbitrary state $|\phi\rangle$. Owing to the choice of $t_1 = 1 > 0$, eigenstates $|\phi\rangle$ of the flake Hamiltonian, $\mathcal{H}_{\{8,3\}}^{(\text{flake})} |\phi\rangle = E |\phi\rangle$, with energy E lying towards the upper end of the energy spectrum have larger contributions $\phi_{n,\ell}$ associated to small values of $\lambda_{n,\ell}$, i.e., slowly oscillating eigenfunctions $u_{n,\ell}(z)$. It is therefore easier to determine ϕ_{ℓ} for those states, while states with smaller energy E are highly oscillatory and require larger $|\ell|$ as well as n .

In practice, our algorithm for calculating the ϕ_{ℓ} for all states $|\phi\rangle$ is set up as follows. To avoid a computationally heavy numerical integration of the individual Wigner-Seitz cell, we choose option (2) discussed above. The vectors $\{|\psi_{n,\ell}^{(2)}\rangle\}_{n>0, \ell \in \mathbb{Z}}$ only depend on the finite lattice, i.e., the flake, and not the Hamiltonian matrix defined on it. Given a flake of the $\{8, 3\}$ lattice (and a compatible choice of bounding radius R), a subset of $\{|\psi_{n,\ell}\rangle\}_{n>0, \ell \in \mathbb{Z}}$ can be precomputed and stored. To do that, we first need to find solutions of Eq. (S28) for the chosen range of angular momentum $\ell \in [\ell_{\min}, \ell_{\max}]$; this is done by a root search in a predefined interval $k \in (0, k_{\max})$. Note that there is some freedom in choosing R due to the discretization; it must lie beyond the outermost site appearing on our disk-shaped flake (i.e., inside the restricted list L_{sites}), but closer than the nearest site of the $\{8, 3\}$ lattice not included in the flake (i.e., not appearing in the slightly larger list \tilde{L}_{sites}). For the system size considered here, we choose $R = 0.991437$. The resulting values $k_{n,\ell}$ allow us to define the corresponding eigenfunctions $u_{n,\ell}(z)$ via Eq. (S25) and consequently

compute $|\psi_{n,\ell}^{(2)}\rangle$. Later, the overlaps $\phi_{n,\ell}^{(2)} = \langle\psi_{n,\ell}^{(2)}|\phi\rangle$ can be efficiently computed for all $|\phi\rangle$, resulting in the energy vs. angular momentum spectrum.

The results of applying the outlined algorithm to states in (and near) the upper energy gap of the hH model and of the rhKM model are shown, respectively, in the two panels of Fig. S7. Let us remark that in the main text Fig. 4(a) we plot essentially the same data as in Supplementary Fig. S7(a). However, as shown in the version of the plot in the supplementary figure, the extracted data are very sharp (one pixel-in- ℓ wide), which would make them hard to see in the small figure panel in the main text. For this reason, we opt in the main text to coarse grain the signal in angular momentum over $(2n_{\max} + 1)$ values of angular momenta as

$$\phi_{\ell}^{(\alpha)} \mapsto \sum_{a=-n_{\max}}^{+n_{\max}} \phi_{\ell+a}^{(\alpha)}. \quad (\text{S40})$$

to improve the visibility. The result of this coarse graining for $n_{\max} \in \{0, 1, 2\}$ (i.e., over 1, 3, resp. 5 adjacent values of ℓ) is shown in Supplementary Fig. S11. The data in main text Fig. 4(a) correspond to $n_{\max} = 2$.

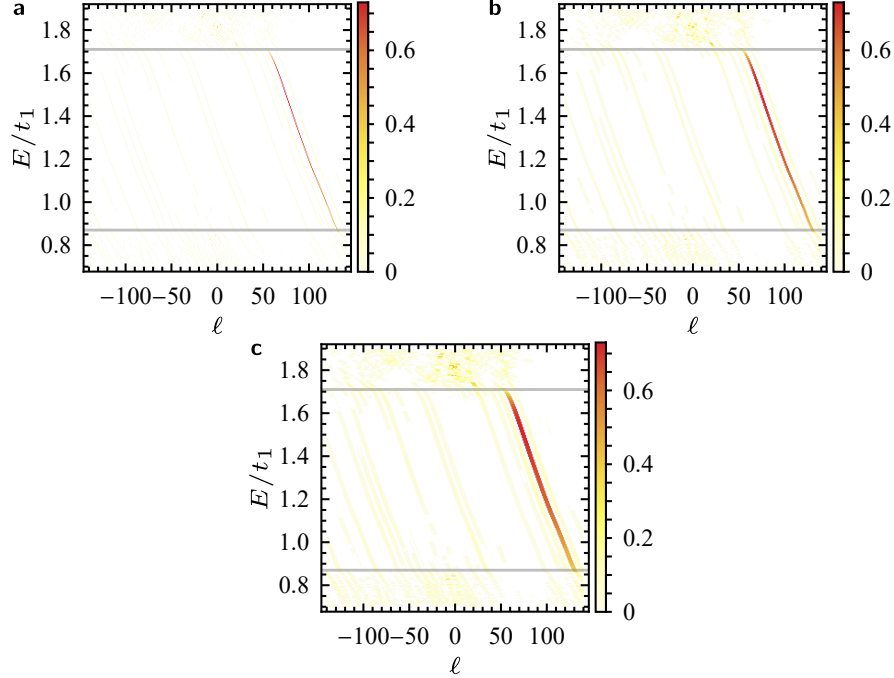


FIG. S11. **Smearing of chiral edge states of the hH model.** **a**, The extracted values of ϕ_{ℓ} for the chiral edge states of the hH model. **b**, The result of smearing the values shown in panel a according to Eq. (S40) with $n_{\max} = 1$ and **c** with $n_{\max} = 2$.

XIV. Group velocity of the chiral edge states in hyperbolic Haldane model

In this supplementary note, we show how the data in Fig. 4(a) and in Fig. 4(b) provide two independent ways to extract the velocity with which the wave packets of topological edge states in the hH model propagate around the flake boundary, allowing for a consistency check of the numerical modelling. We remark that the two figure panels are generated for *different system sizes*; therefore, one should be careful to compare absolute (rather than angular) velocities. Furthermore, the focus is not on quantitative rigor but on qualitative comparison; therefore, we approximate most of the discussed quantities to two significant digits.

We begin with Fig. 4(a), which is computed for a system with $n_{\text{sites}} = 896$, such that the number of Bolza cells is approximately $NUC = 896/16 = 56$. From Eq. (S11) (where we approximate the numerator on the right-hand side by 1) we obtain for the radius R that $1 - R^2 \approx 1/56$. Next, from Eq. (S5) we obtain the perimeter $p \approx 112\pi \approx 350$. We further estimate the angular group velocity as $\omega_{\text{group}} = \Delta E / \Delta \ell$. We read from the data in Fig. 4(a) that across the energy gap $\Delta E \approx 0.83$ and $\Delta \ell \approx 65$, leading to $\omega_{\text{group}} \approx 0.0128$. Multiplying by the perimeter, we obtain the absolute group velocity $v_{\text{group}} \approx \omega_{\text{group}} p \approx 4.5$. (Here, units of length are such that the Gaussian curvature is $K = -4$, cf. Methods. Time is measured in units of \hbar/t_1 ; in numerical modelling we set both \hbar and t_1 to 1.)

On the other hand, the data in Fig. 4(b) are obtained for a system with $n_{\text{sites}} = 1864$. Repeating analogous geometric considerations as above, we find that $NUC = 116.5$, and $1 - R^2 \approx 2/233$. The perimeter of the corresponding system is estimated as $p \approx 233\pi \approx 732$. We read from the data in Fig. 4(b) that the wave packet traverses angular distance $\Delta\alpha \approx 7.5\pi$ in time $\Delta\tau = 4000$, implying angular velocity $\omega = \Delta\alpha / \Delta\tau \approx 0.0059$. Multiplying with the perimeter, we obtain the absolute speed of the wave packet propagation $v = \omega p \approx 4.3$.

We find that the two extracted values of the velocity with which the wave packets propagate along the boundary differ by $\sim 5\%$. This is acceptable agreement within our margin of error, given that several of the discussed quantities (proper choice of R , as well as intervals $\Delta\ell$ and $\Delta\alpha$) can only be extracted up to a few-percent confidence interval.

XV. Phase diagram of the hyperbolic Haldane Bloch Hamiltonian at half-filling and $\Phi = \pi/2$

Recall that for the original Haldane model on the Euclidean honeycomb lattice [30], the inclusion of M drives a trivial energy gap while it is the inclusion of t_2 (at finite flux) that drives the topological gap. The boundary between the trivial and the topological insulating phases is given by the analytic formula $|M/t_2| = 3\sqrt{3}|\sin \Phi|$. In particular, the topological phase of the Euclidean Haldane model persists when M is set to zero.

In this Supplementary Note, we briefly investigate whether a similar competition between the M -driven trivial gap and the t_2 -driven topological gap also occurs at the half-filling for the hyperbolic Haldane Hamiltonian. To that end, we numerically determine [60] the energy gap at half-filling as a function of (M, t_2) for fixed values $t_1 = 1$ and $\Phi = \pi/2$. The result of this analysis is plotted in Supplementary Fig. S12(a), where the red dot indicates the value of model parameters considered throughout the manuscript.

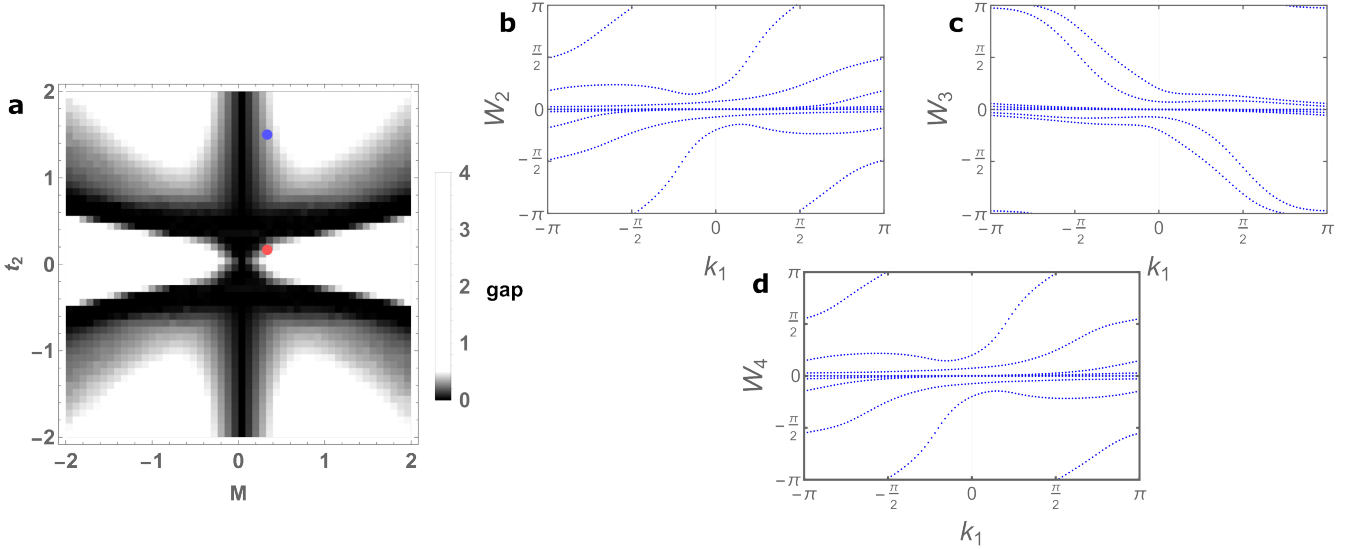


FIG. S12. **Energy gap of the hyperbolic Haldane Bloch Hamiltonian at half-filling.** **a** We set $t_1 = 1$ and $\Phi = \pi/2$, while keeping the parameters M and t_2 variable. Shades of gray indicate the bulk energy gap of the hyperbolic Haldane model as determined by the hyperbolic band theory. Bright tones indicate large values of the gap (expressed in multiples of $t_1 = 1$), while saturated black corresponds to gap closing. Red dot at $M = 1/3$ and $t_2 = 1/6$ corresponds to the choice of parameters considered throughout the manuscript, where the energy gap at half-filling is trivial. The blue dot at $M = 1/3$ and $t_2 = 3/2$ corresponds to the parameters briefly discussed in Supplementary Note XV, where the energy gap at half-filling is associated with non-vanishing Chern numbers C_a, C_b, C_c . **b–d** Wilson-loop spectra for $M = 1/3$ and $t_2 = 3/2$ (blue dot in panel **a**), which indicate $C_a = +2$, $C_b = -2$, and $C_c = +2$.

The first striking feature we observe in Supplementary Fig. S12(a) is that the hyperbolic Haldane model at half-filling, in contrast with the Euclidean one [30], is *gapless* for $M = 0$. We further observe, in resemblance with the Euclidean case, that besides the insulating phase at small values of $|t_2/M|$ there are additional gapped regions occurring at large values of $|t_2/M|$. To determine the band topology of these additional insulating phases, we fix $M = 1/3$ and $t_2 = 3/2$, which correspond to the blue dot in Supplementary Fig. S12(a). We apply the Wilson-loop technique to compute the values of Chern numbers $C_{a,b,c}$ in the insulating phase that occurs at large and *positive* t_2/M . The results of our analysis, plotted in Supplementary Fig. S12(b–d), imply $C_a = +2$, $C_b = -2$, and $C_c = +2$ i.e., the energy gap that occurs at half filling for large t_2/M is topologically non-trivial. Note, however, that the even value of the invariant implies that the corresponding rhKM model for this choice of parameters exhibits trivial values of the \mathbb{Z}_2 -valued invariants ν_a and ν_b . For large and *negative* t_2/M , the signs of the Chern numbers $C_{a,b,c}$ are flipped. We also verified that the second Chern number for these insulating regions is trivial.

Finally, we check that, in contrast to the half-filled case, the bulk energy gap at fillings $f \in \{\frac{5}{16}, \frac{11}{16}\}$ (which correspond to the Chern insulating phases studied in the main text) do not close for $M = 0$. This is illustrated explicitly for $f = \frac{5}{16}$ in Fig. S13 (with the data for $f = \frac{11}{16}$ looking essentially identical). Note that at $M = 0$ the hyperbolic Haldane model acquires an additional symmetry, namely rotation by $\pi/4$ around the center of the Brillouin cell, which permutes momenta as $k_1 \mapsto k_2 \mapsto k_3 \mapsto k_4 \mapsto -k_1$. This symmetry implies that at $M = 0$ (and also for all gapped phases at finite M that extend to $M = 0$) we have

$$C_a := C_{12} = C_{23} = C_{34} = C_{14} =: C_c, \quad (\text{S41})$$

reducing the number of independent Chern numbers to two. [Let us remark that the remaining two Chern numbers could potentially be related by the three-fold rotation around a vertex of the $\{8, 3\}$ lattice. However, as this symmetry is known to act non-orthogonally on the four momentum components [9], we leave a careful investigation of this symmetry for a future study.]

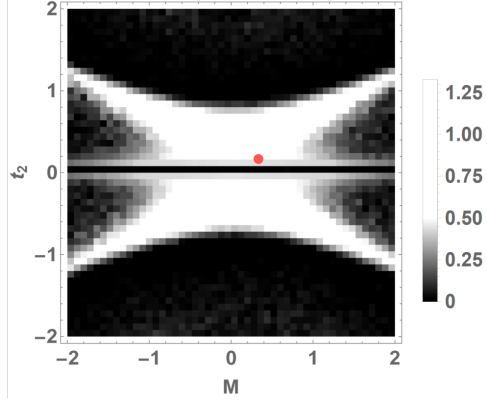


FIG. S13. **Energy gap of the hyperbolic Haldane Bloch Hamiltonian at filling $f = 5/16$.** Two gapped regions can be identified. These regions are related by a sign flip $t_2 \mapsto -t_2$. Since the same change can be interpreted as the action of time-reversal (complex conjugation flips $\Phi \mapsto -\Phi$, which at $\Phi = \pi/2$ corresponds to a sign flip of the purely imaginary t_2 term), the two gapped regions must exhibit opposite sign of all Chern numbers. The red dot indicates the parameter values $t_2 = \frac{M}{2} = \frac{1}{3}$ which are assumed throughout the main text. Since the gapped phase extends to $M = 0$, it follows from an additional $(\pi/4)$ -rotation symmetry that necessarily $C_a = C_c$, cf. Eq. (S41).

References

- [1] Barry Bradlyn, L. Elcoro, Jennifer Cano, M. G. Vergniory, Zhijun Wang, C. Felser, M. I. Aroyo, and B. Andrei Bernevig, “Topological quantum chemistry,” *Nature* **547**, 298–305 (2017).
- [2] Hoi Chun Po, Ashvin Vishwanath, and Haruki Watanabe, “Symmetry-based indicators of band topology in the 230 space groups,” *Nat. Commun.* **8**, 50 (2017).
- [3] Maia G. Vergniory, Benjamin J. Wieder, Luis Elcoro, Stuart S. P. Parkin, Claudia Felse, B. Andrei Bernevig, and Nicolas Regnault, “All topological bands of all nonmagnetic stoichiometric materials,” *Science* **376**, abg9094 (2022).
- [4] Eva Y. Andrei, Dmitri K. Efetov, Pablo Jarillo-Herrero, Allan H. MacDonald, Kin Fai Mak, T. Senthil, Emanuel Tutuc, Ali Yazdani, and Andrea F. Young, “The marvels of moiré materials,” *Nat. Rev. Mater.* **6**, 201–206 (2021).
- [5] Alicia J. Kollár, Mattias Fitzpatrick, and Andrew A. Houck, “Hyperbolic lattices in circuit quantum electrodynamics,” *Nature* **571**, 45 (2019).
- [6] Patrick M. Lenggenhager, Alexander Stegmaier, Lavi K. Upreti, Tobias Hofmann, Tobias Helbig, Achim Vollhardt, Martin Greiter, Ching Hua Lee, Stefan Imhof, Hauke Brand, Tobias Kießling, Igor Boettcher, Titus Neupert, Ronny Thomale, and Tomáš Bzdušek, “Simulating hyperbolic space on a circuit board,” *Nat. Commun.* **13**, 4373 (2022).
- [7] W. Magnus, *Noneuclidean tessellations and their groups* (Academic Press, New York, 1974).
- [8] H. S. M. Coxeter and W. O. J. Moser, *Generators and Relations for Discrete Groups* (Springer Berlin Heidelberg, Berlin, Heidelberg, 1980).
- [9] Joseph Maciejko and Steven Rayan, “Hyperbolic band theory,” *Sci. Adv.* **7**, eabe9170 (2021).
- [10] Sunkyu Yu, Xianji Piao, and Namkyoo Park, “Topological Hyperbolic Lattices,” *Phys. Rev. Lett.* **125**, 053901 (2020).
- [11] Kazuki Ikeda, Shoto Aoki, and Yoshiyuki Matsuki, “Hyperbolic band theory under magnetic field and dirac cones on a higher genus surface,” *J. Phys. Condens. Matter* **33**, 485602 (2021).
- [12] Alexander Stegmaier, Lavi K. Upreti, Ronny Thomale, and Igor Boettcher, “Universality of hofstadter butterflies on hyperbolic lattices,” *Phys. Rev. Lett.* **128**, 166402 (2022).
- [13] Igor Boettcher, Przemysław Bienias, Ron Belyansky, Alicia J. Kollár, and Alexey V. Gorshkov, “Quantum simulation of hyperbolic space with circuit quantum electrodynamics: From graphs to geometry,” *Phys. Rev. A* **102**, 032208 (2020).
- [14] Joseph Maciejko and Steven Rayan, “Automorphic Bloch theorems for hyperbolic lattices,” *Proc. Natl. Acad. Sci. U.S.A.* **119**, e2116869119 (2022).
- [15] Xingchuan Zhu, Jiaojiao Guo, Nikolas P. Breuckmann, Huaiming Guo, and Shiping Feng, “Quantum phase transitions of interacting bosons on hyperbolic lattices,” *J. Phys. Condens. Matter* **33**, 335602 (2021).
- [16] Nikolas P. Breuckmann and Barbara M. Terhal, “Constructions and Noise Threshold of Hyperbolic Surface Codes,” *IEEE Trans. Inf. Theory* **62**, 3731–3744 (2016).
- [17] Igor Boettcher, Alexey V. Gorshkov, Alicia J. Kollár, Joseph Maciejko, Steven Rayan, and Ronny Thomale, “Crystallography of hyperbolic lattices,” *Phys. Rev. B* **105**, 125118 (2022).
- [18] Przemysław Bienias, Igor Boettcher, Ron Belyansky, Alicia J. Kollár, and Alexey V. Gorshkov, “Circuit quantum electrodynamics in hyperbolic space: From photon bound states to frustrated spin models,” *Phys. Rev. Lett.* **128**, 013601 (2022).
- [19] Adil Attar and Igor Boettcher, “Selberg trace formula in hyperbolic band theory,” *Phys. Rev. E* **106**, 034114 (2022).
- [20] Massimo Ruzzene, Emil Prodan, and Camelia Prodan, “Dynamics of elastic hyperbolic lattices,” *Extreme Mech. Lett.* **49**, 101491 (2021).
- [21] Alicia J. Kollár, Mattias Fitzpatrick, Peter Sarnak Sarnak, and Houck. Andrew A., “Line-Graph Lattices: Euclidean and Non-Euclidean Flat Bands, and Implementations in Circuit Quantum Electrodynamics,” *Commun. Math. Phys.* **376**, 1909–1956 (2019).
- [22] Alberto Saa, Eduardo Miranda, and Francisco Rouxinol, “Higher-dimensional Euclidean and non-Euclidean structures in planar circuit quantum electrodynamics,” (2021), arXiv:2108.08854 [quant-ph].
- [23] Tomáš Bzdušek and Joseph Maciejko, “Flat bands and band-touching from real-space topology in hyperbolic lattices,” *Phys. Rev. B* **106**, 155146 (2022).
- [24] Rémy Mosseri, Roger Vogeler, and Julien Vidal, “Aharonov-Bohm cages, flat bands, and gap labeling in hyperbolic tilings,” *Phys. Rev. B* **106**, 155120 (2022).
- [25] Weixuan Zhang, Hao Yuan, Na Sun, Houjun Sun, and Xiangdong Zhang, “Observation of novel topological states in hyperbolic lattices,” *Nat. Commun.* **13**, 2937 (2022).
- [26] Zheng-Rong Liu, Chun-Bo Hua, Tan Peng, and Bin Zhou, “Chern insulator in a hyperbolic lattice,” *Phys. Rev. B* **105**, 245301 (2022).
- [27] Svetlana Katok, *Fuchsian groups* (University of Chicago press, Chicago, 1992).
- [28] Alexei Kitaev, “Periodic table for topological insulators and superconductors,” *AIP Conf. Proc.* **1134**, 22 (2009).
- [29] Shinsei Ryu, Andreas P. Schnyder, Akira Furusaki, and Andreas W. W. Ludwig, “Topological insulators and superconductors: tenfold way and dimensional hierarchy,” *New J. Phys.* **12**, 065010 (2010).
- [30] F. D. M. Haldane, “Model for a Quantum Hall Effect without Landau Levels: Condensed-Matter Realization of the ‘Parity Anomaly’,” *Phys. Rev. Lett.* **61**, 2015–2018 (1988).
- [31] C. L. Kane and E. J. Mele, “ Z_2 Topological Order and the Quantum Spin Hall Effect,” *Phys. Rev. Lett.* **95**, 146802 (2005).
- [32] Alexander B Khanikaev, S Hossein Mousavi, Wang-Kong Tse, Mehdi Kargarian, Allan H MacDonald, and Gennady Shvets, “Photonic topological insulators,” *Nat. Mater.* **12**, 233–239 (2013).
- [33] Gregor Jotzu, Michael Messer, Rémi Desbuquois, Martin Lebrat, Thomas Uehlinger, Daniel Greif, and Tilman Esslinger,

- "Experimental realization of the topological Haldane model with ultracold fermions," *Nature* **515**, 237–240 (2014).
- [34] Yujiang Ding, Yugui Peng, Yifan Zhu, Xudong Fan, Jing Yang, Bin Liang, Xuefeng Zhu, Xiangang Wan, and Jianchun Cheng, "Experimental Demonstration of Acoustic Chern Insulators," *Phys. Rev. Lett.* **122**, 014302 (2019).
- [35] Stefan Imhof, Christian Berger, Florian Bayer, Johannes Brehm, Laurens W Molenkamp, Tobias Kiessling, Frank Schindler, Ching Hua Lee, Martin Greiter, Titus Neupert, and Ronny Thomale, "Topoelectrical-circuit realization of topological corner modes," *Nat. Phys.* **14**, 925 (2018).
- [36] Ching Hua Lee, Stefan Imhof, Christian Berger, Florian Bayer, Johannes Brehm, Laurens W. Molenkamp, Tobias Kiessling, and Ronny Thomale, "Topoelectrical Circuits," *Commun. Phys.* **1**, 39 (2018).
- [37] Tobias Hofmann, Tobias Helbig, Ching Hua Lee, Martin Greiter, and Ronny Thomale, "Chiral Voltage Propagation and Calibration in a Topoelectrical Chern Circuit," *Phys. Rev. Lett.* **122**, 247702 (2019).
- [38] J. Bellissard, A. van Elst, and H. Schulz-Baldes, "The noncommutative geometry of the quantum Hall effect," *J. Math. Phys.* **35**, 5373–5451 (1994).
- [39] Alexei Kitaev, "Anyons in an exactly solved model and beyond," *Ann. Phys.* **321**, 2–111 (2006).
- [40] Raffaello Bianco and Raffaele Resta, "Mapping topological order in coordinate space," *Phys. Rev. B* **84**, 241106(R) (2011).
- [41] Emil Prodan, "Disordered topological insulators: a non-commutative geometry perspective," *J. Phys. A Math. Theor.* **44**, 113001 (2011).
- [42] Huaqing Huang and Feng Liu, "Theory of spin Bott index for quantum spin Hall states in nonperiodic systems," *Phys. Rev. B* **98**, 125130 (2018).
- [43] M. E. Kazaryan, S. K. Lando, and V. V. Prasolov, *Algebraic Curves: Towards Moduli Spaces*, Moscow Lectures, Vol. 2 (Springer, Cham, Switzerland, 2019).
- [44] The Supplemental Material contains supporting data and detailed information about the methods.
- [45] Nan Cheng, Francesco Serafin, James McInerney, Zeb Rocklin, Kai Sun, and Xiaoming Mao, "Band Theory and Boundary Modes of High-Dimensional Representations of Infinite Hyperbolic Lattices," *Phys. Rev. Lett.* **129**, 088002 (2022).
- [46] Anffany Chen, Hauke Brand, Tobias Helbig, Tobias Hofmann, Stefan Imhof, Alexander Fritzsche, Tobias Kießling, Alexander Stegmaier, Lavi K. Uperti, Titus Neupert, Tomáš Bzdušek, Martin Greiter, Ronny Thomale, and Igor Boettcher, "Hyperbolic matter in electrical circuits with tunable complex phases," (2022), arXiv:2205.05106.
- [47] Alexander Altland and Martin R. Zirnbauer, "Nonstandard symmetry classes in mesoscopic normal-superconducting hybrid structures," *Phys. Rev. B* **55**, 1142–1161 (1997).
- [48] Mikio Nakahara, *Geometry, topology and physics*, Graduate student series in physics (Hilger, Bristol, 1990).
- [49] David M. Urwyler, *Hyperbolic Topological Insulator*, Master's thesis, University of Zürich, Switzerland (2021); David M. Urwyler, Patrick M. Lenggenhager, Titus Neupert, and Tomáš Bzdušek, "Topological hyperbolic band insulators," (2022), APS March Meeting 2022, Session N66.
- [50] Alexey A. Soluyanov and David Vanderbilt, "Computing topological invariants without inversion symmetry," *Phys. Rev. B* **83**, 235401 (2011).
- [51] Dominik Gresch, Gabriel Autès, Oleg V. Yazyev, Matthias Troyer, David Vanderbilt, B. Andrei Bernevig, and Alexey A. Soluyanov, "Z2Pack: Numerical implementation of hybrid Wannier centers for identifying topological materials," *Phys. Rev. B* **95**, 075146 (2017).
- [52] Liang Fu, C. L. Kane, and E. J. Mele, "Topological Insulators in Three Dimensions," *Phys. Rev. Lett.* **98**, 106803 (2007).
- [53] Shou-Cheng Zhang and Jiangping Hu, "A Four-Dimensional Generalization of the Quantum Hall Effect," *Science* **294**, 823–828 (2001).
- [54] Dan S. Borgnia, Alex Jura Kruchkov, and Robert-Jan Slager, "Non-hermitian boundary modes and topology," *Phys. Rev. Lett.* **124**, 056802 (2020).
- [55] Nobuyuki Okuma, Kohei Kawabata, Ken Shiozaki, and Masatoshi Sato, "Topological Origin of Non-Hermitian Skin Effects," *Phys. Rev. Lett.* **124**, 086801 (2020).
- [56] Sebastian Weidemann, Mark Kremer, Tobias Helbig, Tobias Hofmann, Alexander Stegmaier, Martin Greiter, Ronny Thomale, and Alexander Szameit, "Topological funneling of light," *Science* **368**, 311–314 (2020).
- [57] Tobias Hofmann, Tobias Helbig, Frank Schindler, Nora Salgo, Marta Brzezińska, Martin Greiter, Tobias Kiessling, David Wolf, Achim Vollhardt, Anton Kabashi, Ching Hua Lee, Ante Bilušić, Ronny Thomale, and Titus Neupert, "Reciprocal skin effect and its realization in a topoelectrical circuit," *Phys. Rev. Research* **2**, 023265 (2020).
- [58] T. Helbig, T. Hofmann, S. Imhof, M. Abdelghany, T. Kiessling, L. W. Molenkamp, C. H. Lee, A. Szameit, M. Greiter, and R. Thomale, "Generalized bulk-boundary correspondence in non-hermitian topoelectrical circuits," *Nat. Phys.* **16**, 747–750 (2020).
- [59] Chenwei Lv, Ren Zhang, Zhengzheng Zhai, and Qi Zhou, "Curving the space by non-Hermiticity," *Nat. Commun.* **13**, 2184 (2022).
- [60] David M. Urwyler, Patrick M. Lenggenhager, Igor Boettcher, Ronny Thomale, Titus Neupert, and Tomáš Bzdušek, "Data and code for: Hyperbolic topological band insulators," (2022), DOI: <https://doi.org/10.5281/zenodo.6380568>.